

# Unsteady Pressure Acquisition on the 1.75% Scale SLS Block 1B Cargo Liftoff Configuration

*L. J. Mears, P. R. Shea, J. G. Collins, M. A. Walker, S. L. Langston, and J. T. Pinier  
Langley Research Center, Hampton, Virginia*

*P. Nikoueeyan, M. Perry, J. Strike, B. Wimpenny, and M. Hind  
Resono Pressure Systems, Inc., Laramie, Wyoming*

*J. W. Naughton  
University of Wyoming, Laramie, Wyoming*

## NASA STI Program... in Profile

Since its founding, NASA has been dedicated to the advancement of aeronautics and space science. The NASA scientific and technical information (STI) program plays a key part in helping NASA maintain this important role.

The NASA STI Program operates under the auspices of the Agency Chief Information Officer. It collects, organizes, provides for archiving, and disseminates NASA's STI. The NASA STI Program provides access to the NASA Aeronautics and Space Database and its public interface, the NASA Technical Report Server, thus providing one of the largest collections of aeronautical and space science STI in the world. Results are published in both non-NASA channels and by NASA in the NASA STI Report Series, which includes the following report types:

- **TECHNICAL PUBLICATION.** Reports of completed research or a major significant phase of research that present the results of NASA programs and include extensive data or theoretical analysis. Includes compilations of significant scientific and technical data and information deemed to be of continuing reference value. NASA counterpart of peer-reviewed formal professional papers, but having less stringent limitations on manuscript length and extent of graphic presentations.
- **TECHNICAL MEMORANDUM.** Scientific and technical findings that are preliminary or of specialized interest, e.g., quick release reports, working papers, and bibliographies that contain minimal annotation. Does not contain extensive analysis.
- **CONTRACTOR REPORT.** Scientific and technical findings by NASA-sponsored contractors and grantees.

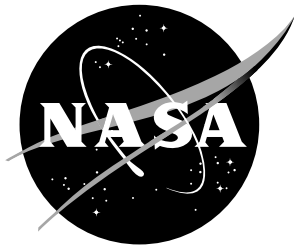
- **CONFERENCE PUBLICATION.** Collected papers from scientific and technical conferences, symposia, seminars, or other meetings sponsored or co-sponsored by NASA.
- **SPECIAL PUBLICATION.** Scientific, technical, or historical information from NASA programs, projects, and missions, often concerned with subjects having substantial public interest.
- **TECHNICAL TRANSLATION.** English-language translations of foreign scientific and technical material pertinent to NASA's mission.

Specialized services also include organizing and publishing research results, distributing specialized research announcements and feeds, providing information desk and personal search support, and enabling data exchange services.

For more information about the NASA STI Program, see the following:

- Access the NASA STI program home page at <http://www.sti.nasa.gov>
- E-mail your question to [help@sti.nasa.gov](mailto:help@sti.nasa.gov)
- Phone the NASA STI Information Desk at 757-864-9658
- Write to:  
NASA STI Information Desk  
Mail Stop 148  
NASA Langley Research Center  
Hampton, VA 23681-2199

NASA/TM-20220002633



# Unsteady Pressure Acquisition on the 1.75% Scale SLS Block 1B Cargo Liftoff Configuration

*L. J. Mears, P. R. Shea, J. G. Collins, M. A. Walker, S. L. Langston, and J. T. Pinier  
Langley Research Center, Hampton, Virginia*

*P. Nikoueeayan, M. Perry, J. Strike, B. Wimpenny, and M. Hind  
Resono Pressure Systems, Inc., Laramie, Wyoming*

*J. W. Naughton  
University of Wyoming, Laramie, Wyoming*

National Aeronautics and  
Space Administration

Langley Research Center  
Hampton, Virginia 23681-2199

---

March 2022

## Acknowledgments

We gratefully acknowledge the assistance of the 14- by 22-Foot Subsonic Tunnel facility staff in conducting these experiments.

The use of trademarks or names of manufacturers in this report is for accurate reporting and does not constitute an official endorsement, either expressed or implied, of such products or manufacturers by the National Aeronautics and Space Administration.

Available from:

NASA STI Program / Mail Stop 148  
NASA Langley Research Center  
Hampton, VA 23681-2199  
Fax: 757-864-6500

## Abstract

Time-varying pressure on the core of the Space Launch System (SLS) Block 1B Cargo vehicle was acquired using instrumentation typically used for steady, time-averaged pressure. Resono Pressure Systems, Inc. in partnership with the University of Wyoming have developed a unique hardware and software system for measuring unsteady pressure, which was implemented in a large-scale wind tunnel test through a nonreimbursable Space Act Agreement with NASA. The technique was applied to 12 pressure ports on the 1.75% scale SLS wind tunnel model. Tubing lengths of approximately 14 inches separated the pressure transducer module from the pressure taps on the model surface, and surface-mount validation sensors (Kulites) were installed in close proximity to 5 of the 12 pressure ports. Up to about 500 Hz, the frequency response of pressure fluctuations agreed to within 1 dB of amplitude and  $10^\circ$  of phase difference compared to the simultaneously-acquired surface-mount transducers. Sample results using the reconstructed pressure from the full azimuthal ring of taps are presented.

# Contents

<b>1</b>	<b>Introduction</b>	<b>4</b>
<b>2</b>	<b>Experimental Methods</b>	<b>5</b>
2.1	Wind Tunnel Facility . . . . .	5
2.2	SLS Block 1B Cargo Model . . . . .	5
2.3	Model Configurations . . . . .	6
2.4	Unsteady Pressure Measurements . . . . .	6
2.5	Validation Sensors . . . . .	12
<b>3</b>	<b>Data Analysis Methods</b>	<b>13</b>
3.1	Pressure Reconstruction . . . . .	13
3.2	Spectral Analysis Methods . . . . .	13
<b>4</b>	<b>Results</b>	<b>14</b>
4.1	Verification of Unsteady Pressure . . . . .	14
4.1.1	Time-domain Comparison . . . . .	14
4.1.2	Power Spectral Density (PSD) . . . . .	16
4.1.3	Magnitude-squared Coherence ( $\gamma^2$ ) . . . . .	18
4.1.4	Frequency Response Function (FRF) . . . . .	18
4.2	Flow Physics . . . . .	19
4.2.1	Pressure Intensity . . . . .	20
4.2.2	Power Spectral Density (PSD) . . . . .	23
<b>5</b>	<b>Conclusions and Recommendations</b>	<b>31</b>
	<b>Appendix A Potential Effects of Aliasing</b>	<b>34</b>
	<b>Appendix B Noise Analysis</b>	<b>36</b>

# Nomenclature

## Latin symbols

$C'_p$	Fluctuating pressure coefficient, $p'/q_\infty$
$D$	SLS core diameter
$f$	Frequency, Hz
$f_s$	Sampling frequency, Hz
$h/L$	Elevation of the launch vehicle relative to the height of the launch tower
$M_\infty$	Freestream Mach number
$p$	Static pressure, psi
$p'$	Fluctuating pressure component, psi
$p_0$	Pressure on model surface, psi
$\hat{p}_0$	Pressure measured by the ESP (reconstructed), psi
$p_r$	Pressure measured at the ESP (raw), psi
$q_\infty$	Freestream dynamic pressure, psf
$Re_D$	Reynolds number based on core diameter, $u_\infty D/\nu$
$St_D$	Strouhal number based on core diameter, $fD/u_\infty$
$u_\infty$	Freestream velocity, ft/s

## Greek symbols

$\gamma^2$	Magnitude-squared coherence
$\theta$	Azimuthal pressure tap position with respect to $\psi_{azm}$ , degrees
$\nu$	Kinematic viscosity
$\sigma$	Root-mean-square fluctuating pressure normalized by dynamic pressure
$\phi$	Phase lag, degrees
$\tau_{delay}$	Filter delay, sec
$\psi_{azm}$	Model rotation (azimuthal wind direction), degrees

## Acronyms and Abbreviations

14x22	NASA Langley 14- by 22-Foot Subsonic Tunnel
C1, C2, C3	Vehicle and ML-2 configurations (see §2.3)
CPSD	Cross-power spectral density
ESP	Electronic pressure scanner manufactured by TE Connectivity
FIR	Finite Impulse Response
FRF	Frequency Response Function
ML-2	Mobile launcher for SLS Block 1B
NI DAQ	National Instruments Data Acquisition System
PSD	Power spectral density, $\text{psi}^2/\text{Hz}$
SAA	Space Act Agreement
SLS	Space Launch System
SNR	Signal-to-noise ratio

# 1 Introduction

Unsteady pressure measurements provide important insight into the flow physics of a flight environment. Such measurements can be used to validate numerical simulations or to identify whether a boundary layer is attached or separated at specific regions on a vehicle surface. This is typically achieved in wind tunnels by employing surface-mounted pressure transducers at key locations on a model. If extremely high spatial resolution is desired or where structural factors inhibit the installation of surface-mounted pressure transducers, individual pressure taps can be connected to a remote transducer module via lengths of flexible tubing [1,2]. This methodology represents potential cost-savings over discrete sensors at the expense of additional data processing to remove the tube's influence - namely signal attenuation, lag, and resonance [3]. Although straightforward to model analytically using linear acoustics theory, it is not a trivial exercise in practice due to the amplification of noise at high frequencies and sensitivity to geometric parameters [4].

Through a nonreimbursable Space Act Agreement (SAA) between NASA and the University of Wyoming, unsteady pressure data were collected in the NASA Langley 14- by 22-Foot Subsonic Tunnel (14x22) on the Space Launch System (SLS) Block 1B Cargo vehicle. This research effort aimed to demonstrate the effectiveness of a unique acquisition system developed by Resono Pressure Systems, Inc., which uses traditional static pressure taps and tubing routed to a TE Connectivity electronic pressure scanner (ESP) module to sample 12 channels concurrently. Postprocessing included a combination of analytical and empirical system characterization to reduce the effects of attenuation, temporal lag, and resonance introduced by the lengths of pressure tubing, which has previously been applied to experiments on wind tunnel blades and shock tubes [4-6].

The present measurements were performed during a larger 14x22 wind tunnel test campaign to characterize the liftoff flight environment of the SLS [7]. Minimal investment in testing equipment and time were required to incorporate the additional goal of demonstrating the reconstruction of pressure signals. Pressure fluctuations were recorded using an ESP acquisition system provided by Resono, and validation is performed using simultaneously acquired high-fidelity piezoresistive pressure sensors (Kulites) mounted on the surface of the wind tunnel model close to the pressure taps. The selection of Kulites was not ideal because of the high pressure range (15 psi), but provided adequate validation in cases with strong pressure fluctuations and high signal-to-noise ratio (SNR). The primary goal of this research effort is to evaluate the technology developed by the University of Wyoming and Resono and to make recommendations for improvements or future use of the acquisition system. The secondary goal is to identify any interesting flow features present during the wind tunnel test and to provide an unsteady validation dataset for the SLS Block 1B vehicle.

This report is organized into three primary sections. The test article, facility, and instrumentation will be discussed in Section 2. Analysis methods for comparing the spectral content of the measurements and frequency response characterization are discussed in Section 3. Experimental results include validation of the reconstructed pressure signals measured by the ESP, which is the focus of Section 4.1,

and observations related to the flow physics, discussed in Section 4.2.

## 2 Experimental Methods

### 2.1 Wind Tunnel Facility

The experiment was performed at the NASA Langley Research Center 14- by 22-Foot Subsonic Tunnel. This closed-circuit, atmospheric-pressure wind tunnel is capable of operating in different test-section configurations, and all present tests were conducted using the closed test section walls. With the walls closed, the test section dimensions are 14.5 ft high by 21.75 ft wide by 50 ft long. The flow in the settling chamber is conditioned by a flow-straightening honeycomb, four square-mesh screens with a mesh count of 10 per inch and 64% open area, and a tunnel contraction area of 9 to 1. Previous studies have reported turbulence intensities between 0.05-0.07% of the freestream velocity at a dynamic pressure ( $q_\infty$ ) of 50 psf [8]. No efforts were made to simulate turbulence levels in realistic atmospheric boundary layers. Further details about the tunnel can be found in Gentry et al. [9].

The runs are acquired using point-pause motion of the test article. Once pressure readings and force and moment readings have settled at a specified dynamic pressure and vehicle orientation, acquisition is initiated. Temperature variations resulted in a range of Mach and Reynolds numbers during testing. For nominal  $q_\infty = 50$  psf tests, the Mach number ( $M_\infty$ ) varied between 0.1846 and 0.1871. The dynamic pressure, calculated by subtracting the static pressure measured at the wall in the test section from the total pressure in the settling chamber, typically varies by 0.3% during data acquisition. Variations in outdoor temperature during this test campaign produced test section temperatures ranging from 70°F to 105°F, with unit Reynolds number at  $q_\infty = 50$  psf ranging from  $1.1 \times 10^6/\text{ft}$  to  $1.25 \times 10^6/\text{ft}$  ( $Re_D = 0.53 \times 10^6$  to  $0.60 \times 10^6$ ).

### 2.2 SLS Block 1B Cargo Model

Although the model geometry and full test data are Controlled Unclassified Information (CUI), the limited dataset used for the technology demonstration described in this report has been deemed Fundamental Research and is not subject to Export Control. The exact location of the pressure taps is considered sensitive information and has not been included. Only those details required to interpret the pressure data have been included.

The 1.75% scale model consists of two primary components: a centerbody core with an attached pair of solid rocket boosters (SRBs) - together comprising the SLS Block 1B Cargo launch vehicle - and a mobile launch platform (ML-2) that provides support to the vehicle prior to liftoff. The launch vehicle with the ML-2 is pictured in Fig. 1. Distributed roughness (#80 grit carborundum) is adhered to the entire vehicle surface in order to promote transition to turbulence. The impact on the grit application is unknown. The gap between the vehicle and the closest face of the ML-2 is approximately 1.28 core diameters ( $D$ ). The movable umbilicals that interface with the launch vehicle have been painted red (shown here in the retracted

configuration), while the tower structure is painted black. The current effort focuses on a single azimuthal array of pressure taps on the vehicle centerbody away from the SRBs; the approximate location of this array is shown with a cyan band in Fig. 1.

The vehicle is mounted on a sting with motorized height adjustment relative to the launch tower and tests were conducted at nominal height increments of  $h/L = 0.1$  over a range of  $h/L = -0.003$  to  $0.876$ , where  $h$  equals the vertical elevation of the vehicle and  $L$  is the height of the launch tower, as shown in Fig. 2. Due to the selected reference point on the vehicle,  $h/L = -0.003$  is the lowest height tested, where the SLS vehicle remains prior to liftoff.

The vehicle and launch tower are mounted on a yaw table in the liftoff configuration perpendicular to the wind tunnel floor. In this configuration, the vehicle's angle of attack is  $90^\circ$  and the freestream flow simulates incoming ground winds. Figure 3 shows the definition of wind direction,  $\psi_{azm}$ , ranging from  $0^\circ$  and  $360^\circ$  with respect to the vehicle and ML-2. The cardinal directions correspond to the geographical orientation of Launch Pad 39-B in Cape Canaveral, Florida, where the ML-2 lies directly north of the SLS vehicle. Tests were conducted using  $\psi_{azm}$  increments of  $10^\circ$ , resulting in 33 angles, since  $80^\circ$ ,  $90^\circ$ , and  $100^\circ$  were unattainable (gray region in Fig. 3) due to mechanical constraints of the yaw table.

### 2.3 Model Configurations

Three sequences of testing were conducted, each consisting of similar flow conditions with changes to the model configuration, shown in Fig. 4. The vehicle configurations are as follows: C1, with the Mobile Launch tower and umbilicals retracted, (Fig. 4(a)); C2, with the Mobile Launch tower and umbilicals deployed (Fig. 4(b)); and C3, with the Mobile Launch tower removed (Fig. 4(c)). Umbilicals are five support structures connecting the ML-2 and the launch vehicle that fall away from the vehicle shortly before liftoff, which are shown in red in Fig. 4(a) and (b). Deployment of the umbilicals simply means that the parts are moved away from the tower and are positioned very close to the vehicle surface - in reality, the umbilicals attach to the launch vehicle, but for purposes of force and moment testing, a small clearance gap is maintained between the parts. The ML-2 was completely removed from the ground plane for configuration C3, as shown in Fig. 4(c).

### 2.4 Unsteady Pressure Measurements

The purpose of the test is to determine whether unsteady, time-varying pressure data could be accurately measured using equipment typically used for steady, time-averaged pressure. Resono Pressure Systems, Inc., provided the unsteady pressure acquisition equipment for the test, which included a proprietary data acquisition system for communicating with the ESP pressure scanner module and an NI CompactRIO chassis with two NI-9239 high-speed voltage acquisition cards to sample pressure signals from the Kulite validation sensors. The pressure scanner used was a TE Pressure Systems Model ESP-32HD module with a full-scale range of 1 psi. 12 of the 32 available pressure scanner ports were connected to pressure taps on the model surface in an azimuthal ring (blue circles in Fig. 5) at a single axial location

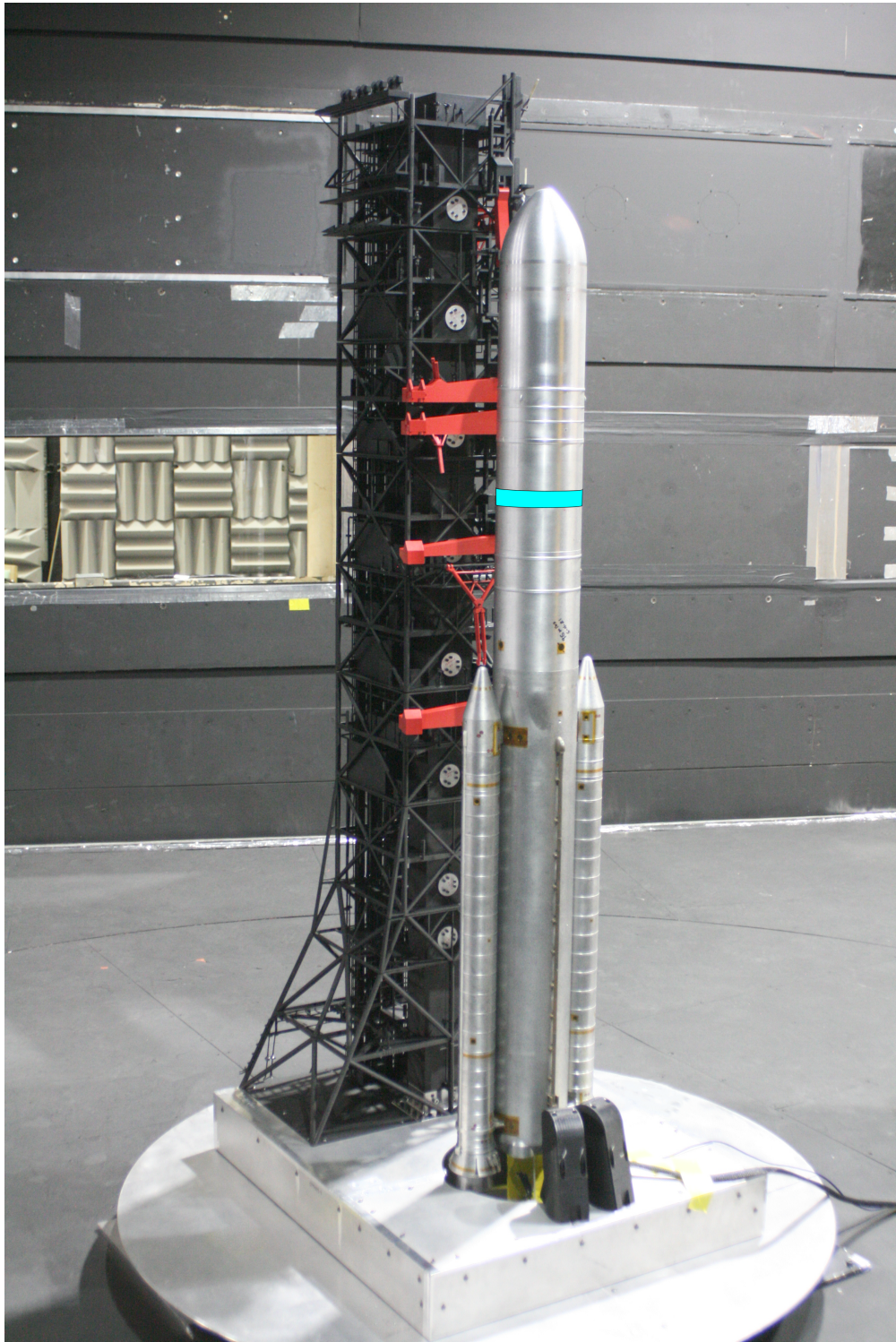


Figure 1. SLS Block 1B Cargo 1.75% scale model with mobile launch tower installed in the closed test section of the Langley 14x22 wind tunnel. The approximate axial location of the pressure tap array on the launch vehicle is indicated in cyan.

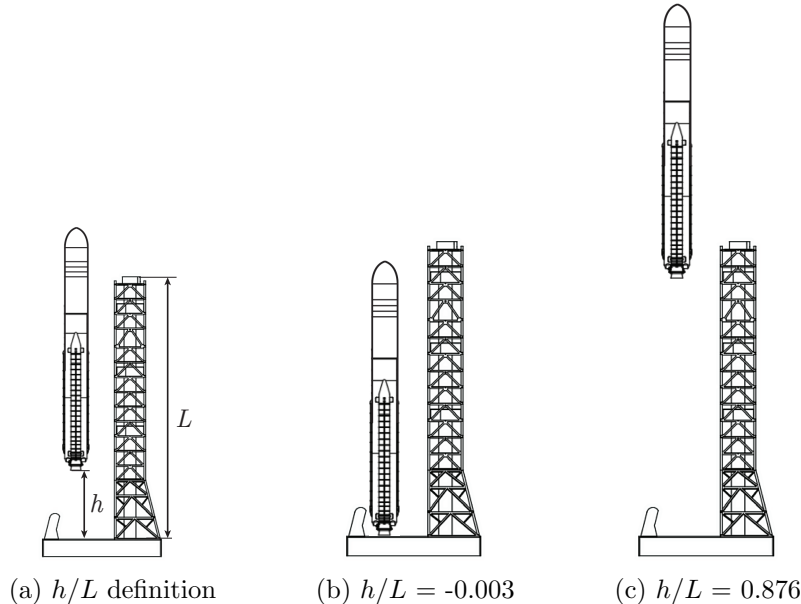


Figure 2. Launch vehicle elevation with respect to the ML-2 height ( $h/L$ ) and limiting cases in the present test campaign.

on the model. Although the pressure ports are located above the SRBs, as shown in Fig. 1, the outline of the SRBs are shown in Fig. 5 for reference. The pressure ports are sequentially numbered from 1 to 12, and Ports 1, 4, 9, 10, and 11 have corresponding comparison Kulites (yellow triangles in Fig. 5). The tubing length between the 12 pressure taps and the ESP scanner was approximately 14 inches total, which comprised of 6 inches of stainless steel tubing, 8 inches of 0.040 inch diameter Tygon tubing, and an adapter with short lengths of 0.065 inch diameter tubing to connect to the ESP module.

The ESP module was connected to the facility calibration line and five-point static calibrations were performed before and after testing. After model build-up, the module was connected to a separate calibration line with a leak, so in situ static calibration of the ESP transducers was not possible until the second phase of testing, when this line could be accessed. Each channel demonstrated highly stable sensitivity values, and the highest deviation in sensitivity among three calibrations was less than 0.4%.

An essential step in determining the accurate transfer function for each transducer is an empirical correction to the analytical transfer function that accounts for nonidentical tubing geometries [4,6]. The frequency response characteristics can be optimized to increase the cutoff frequency of the Wiener filter and preserve as much of the recorded frequency content as possible. This procedure is termed tubing characterization, wherein a known pressure impulse is applied to the surface of the model at the pressure tap and simultaneously recorded at the transducer at the end of the length of tubing. The ESP and applied pressure are sampled simultaneously at a rate of 10 kHz during this process. Short (2 ms) and long (200 ms) step impulses are

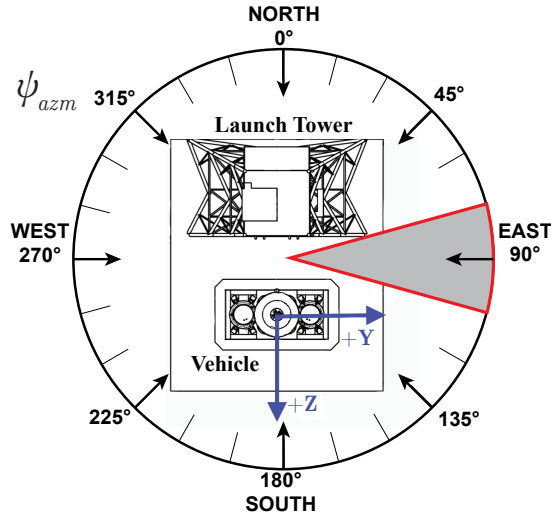
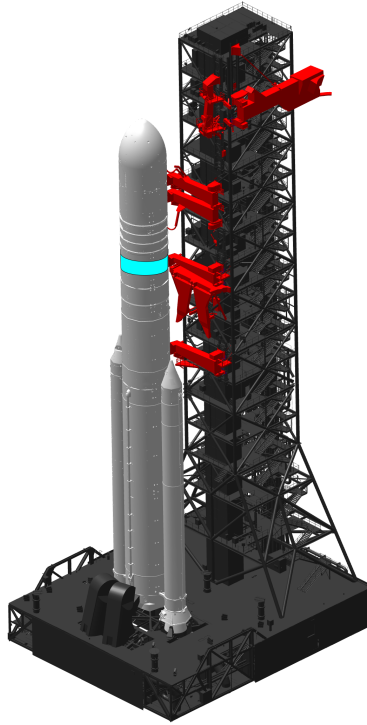


Figure 3. Top-down view of the model with wind direction  $\psi_{azm}$  definition. Angles 80°-100° (gray sector) were not attainable.

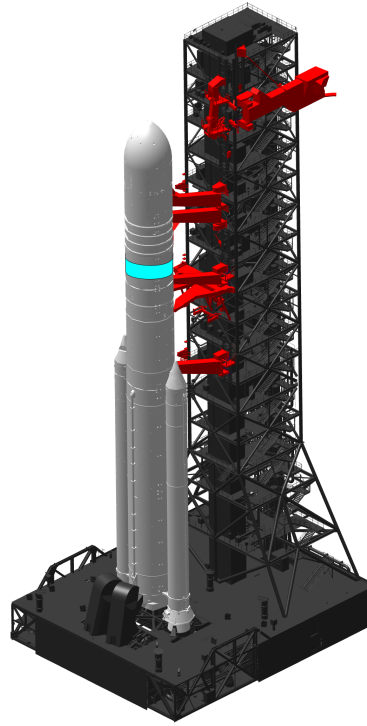
applied using a fast-acting valve, producing the frequency response shown in Fig. 6. The pressure applied to the port ( $p_0$ ) is shown as a dashed black line, while the raw recorded pressure by the ESP ( $p_r$ ) is plotted as a solid red line. The reconstructed signal ( $\hat{p}_0$ ) is the result of the inverse transfer function applied to  $p_r$ , and closely approximates the original signal,  $p_0$ . The magnitude ( $|\frac{\hat{p}_0}{p_0}|$ ) and phase response ( $\phi(\frac{\hat{p}_0}{p_0})$ ) of the reconstructed signal provide a quantitative evaluation of the accuracy of the reconstruction method to match the applied impulse. The mechanical opening of the valve limits the maximum frequency excited by the impulse, which is near 400 Hz, and so the noise observed in the frequency response function (FRF) above 400 Hz is due to absence of appreciable signal content at these frequencies.

During testing, the ESP module sampled pressures at a rate of 2,000 Hz per channel for a duration of 6 seconds, resulting in 12,000 total samples. The 6 second record length was chosen in order not to interfere with concurrent force and moment testing, which recorded for 8 seconds and automatically moved the model to the next position when acquisition was complete. A sensitivity study was conducted with a single 60-second-long acquisition to assess whether this record length provided adequate convergence of the spectral content of the flow. The data are processed for record lengths of 3, 6, 15, 30, and 60 seconds, as shown in Fig. 7. A record length of 6 seconds, shown in red, adequately captures the spectral distribution of energy observed, although there is higher noise compared with the fully-converged power spectral density (PSD) using record lengths of 30 seconds or higher.

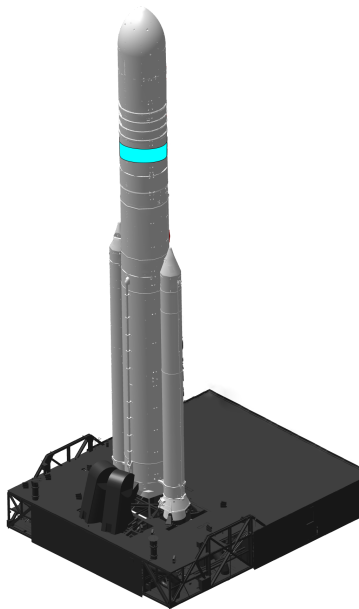
Due to the operation of the ESP, which digitally multiplexes the signal after acquisition, no antialiasing filtering is applied during digitization. A study on the potential effects of aliasing on the signals is included in Appendix A. Additionally, the ESP modules do not sample individual channels simultaneously, instead, each subsequent port is sampled at 40  $\mu$ s intervals within the 500  $\mu$ s sampling period.



(a) C1: umbilicals retracted



(b) C2: umbilicals deployed



(c) C3: vehicle alone

Figure 4. Model configurations for SLS Block 1B Cargo and ML-2. The approximate axial location of the pressure tap array on the launch vehicle is indicated in cyan.

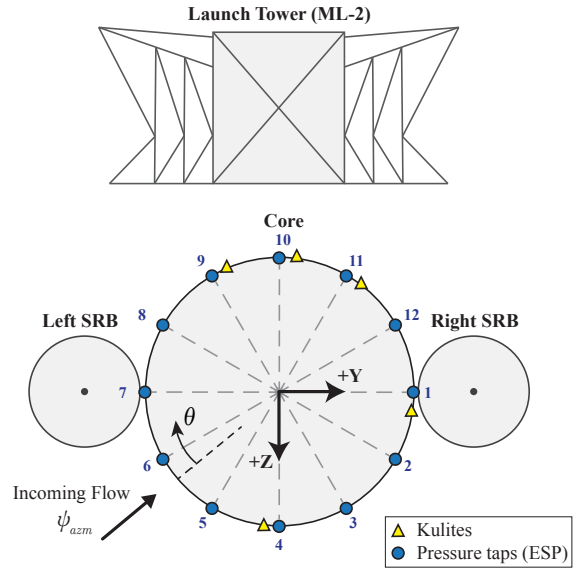


Figure 5. Top-down view of the model showing the location of 12 pressure taps and 5 surface-mounted Kulites spaced  $3^\circ$  from the taps (ML-2 not to scale).

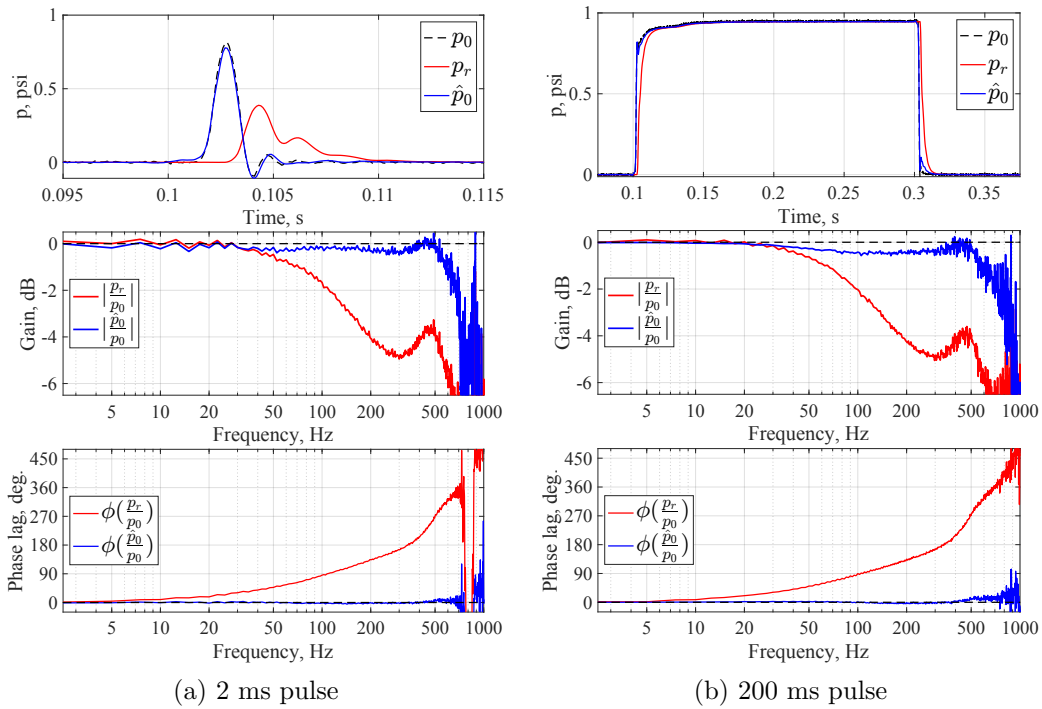


Figure 6. Time response and FRF at a single pressure port for two pulse lengths used in tubing characterization.

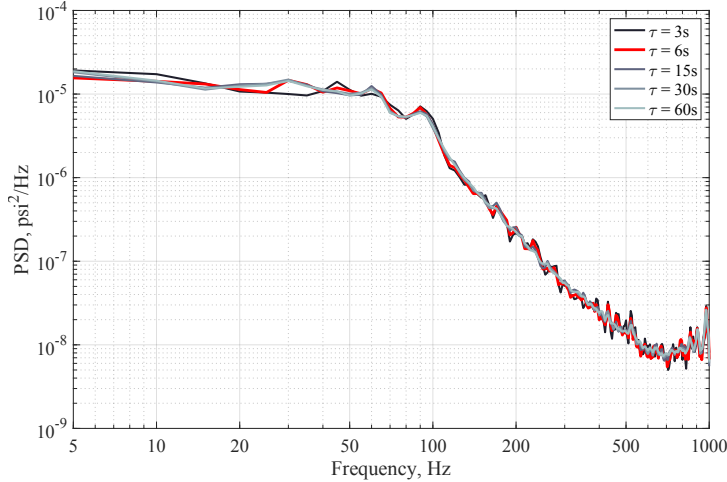


Figure 7. Spectral convergence for a single port using different record lengths. All data shown in this report were recorded for 6 seconds.

## 2.5 Validation Sensors

Signals from surface-mounted, piezoresistive pressure transducers (Kulites) are simultaneously acquired to provide a validation for the pressure recorded using lengths of tubing connected to the ESP module. The 5 sensors were placed as close as possible to the static pressure taps to provide a validated pressure reading at Ports 1, 4, 9, 10, and 11 (Fig. 5), and the sensors were installed  $3^\circ$  away from corresponding pressure taps. The voltages are recorded at 50 kHz using two NI-9239 modules (for CompactRIOs) that apply sigma-delta antialiasing filters with a cutoff frequency of 22.5 kHz [10]. The equation for time delay of the filter is provided as

$$\tau_{delay} = \left(40 + \frac{5}{512}\right) / f_s + 3.3\mu s \quad (1)$$

which results in a delay of  $803.5 \mu s$  when the sampling rate is 50 kHz. The alias-free passband frequency is 0 - 22.65 kHz. Each channel was sampled simultaneously for a duration of 6 seconds, yielding a total of 300,000 samples per channel.

Ports 1 and 4 were instrumented with XCL-19-IA-072 Kulites, while Ports 9, 10, and 11 were instrumented with XCL-31-IA-072 Kulites. The 15 psi differential pressure transducers had a full-scale range of 30 psi and were preamplified to provide a nominal static sensitivity of 165 mV/psi. This sensor pressure range was much higher than required for the test, since the peak pressure fluctuations measured were on the order of 0.2 psi, or 33 mV. The relatively low sensitivity was not desirable, and instrument noise became a significant concern during testing and is discussed in Appendix B. The noise signature also differed between the XCL-19 (Ports 1 and 4) and XCL-31 (Ports 9-11) Kulites due to differences in the in-line amplifiers, resulting in instrumentation noise obscuring the lowest pressure fluctuations measured. Excitation voltage for the transducers was provided by the 12V common power supply of the Resono system to minimize potential ground loops.

The ESP module and Kulites were calibrated in situ by applying a range of known pressures to the reference line of each sensor and recording the output voltage through the data acquisition system. Because the reference line was shared with facility equipment, the transducers were calibrated over the range of  $\pm 0.16$  psi. Although the calibrated range is lower than the full range of the sensors, the majority of test conditions did not exceed the calibration bounds. A linear regression was then applied to each sensor calibration data set and the sensitivity was set equal to the slope of the curve fit.

### 3 Data Analysis Methods

#### 3.1 Pressure Reconstruction

The reconstruction of pneumatically distorted pressure fluctuations at the model surface follows the theory developed by Bergh and Tijdeman [11] and Wiener deconvolution algorithm developed by Whitmore and Wilson [12]. The length of pressure tubing is modeled as a system of acoustic ducts with an associated transfer function that describes how pressure fluctuations applied at the surface of the model are measured by the ESP module downstream of the tubing. The temperature and pressure measured during wind tunnel runs are used to update the sonic velocity and dynamic viscosity used by the inverse transfer function for each unsteady pressure acquisition, but changes in humidity were not considered. The methodology has been applied to previous wind tunnel tests by Resono; additional details appear in Refs. [4, 6].

#### 3.2 Spectral Analysis Methods

Since the ESP and fast-response transducer measurements are acquired at different time scales (sampling frequencies), the ESP time histories are digitally upsampled to match Kulite acquisition using the Matlab function `resample` with a filter of order 10,000 [13]. The high filter order is required to produce an equivalent spectral distribution for both the original and upsampled signals up to the maximum resolvable frequency, 1,000 Hz, with a maximum difference in PSD below 0.2% between 0 Hz and 990 Hz, although this comes at additional computational expense to apply the filter. The last few data points between 990 Hz and 1000 Hz are more strongly affected by the filtering, with maximum error below 20%. A time delay between signals is introduced during acquisition due to sigma-delta filtering in the NI DAQ modules ( $\tau_{delay}$ ), as well as a difference in acquisition start times for the two sensors introduced by the necessary NI drivers. Timestamps are recorded with submicrosecond accuracy by the NI Sync master clock in the CompactRIO system for both ESP and Kulite signals, and this time delay is accounted for in each case and the overlapping samples are used for calculation of the FRF. The magnitude ratio and phase are considered with respect to the Kulite signal, which is assumed to provide an accurate measurement of the pressure fluctuations over the frequency range 0 - 1,000 Hz.

This permits FRF calculation of the ESP and fast-response transducer measurements using a cross-power spectral density (CPSD) approach. Typical spectra for ESP measurements are calculated using Welch’s periodogram method with averaging block sizes of 400 samples, resulting in frequency resolution of 5 Hz and a total number of 30 averages with Hanning windowing. The FRF are calculated using the upsampled ESP and Kulite data, and are calculated with averaging block sizes of 5,000 samples, resulting in frequency resolution of 10 Hz and a total number of 55 averages with Hanning windowing.

## 4 Results

### 4.1 Verification of Unsteady Pressure

The primary goal of this study is to evaluate whether measuring unsteady pressures with an ESP module and short ( $\sim 1$  foot) lengths of pressure tubing provides accurate results using empirically-informed inverse transfer methods. This is accomplished by directly comparing the signals measured by the ESP with unsteady pressure measured using surface-mounted pressure transducers in the frequency domain. For evaluation purposes, the time history of several example cases show how the pressure reconstruction effectively captures pressure fluctuations present on the model surface. All of the results shown in Section 4.1 involve the launch vehicle with ML-2 and umbilicals in the retracted position (C1).

#### 4.1.1 Time-domain Comparison

The first step in validating the corrected ESP measurements with those from neighboring fast-response pressure transducers is to plot the signals in time history and visually assess that the reconstructed signals from the ESP are appropriately capturing the pressure fluctuations on the surface. Two cases are selected that highlight the difference in flow physics observed in different test conditions. Noise becomes significant in the measurements for lower dynamic pressure, so the primary test conditions will be at the highest dynamic pressure tested,  $q_\infty = 50$  psf. Instrument noise also substantially affects two out of the five Kulites (installed at Ports 1 and 4), and this will also be observed in poor relationship in the time histories between reconstructed ESP signals and Kulites. None of the signals will be perfectly correlated due to the small spatial difference in the two sensor locations that are plotted together.

The signals included in Figs. 8 and 9 are the Kulite (black solid line), raw (uncorrected) ESP (red dotted line), and reconstructed ESP (blue solid line). Three cases are selected, each at  $q_\infty = 50$  psf and varying  $\psi_{azm}$  angles, where the vehicle experiences varying levels of intensity of pressure fluctuations on the surface. Note that the y-axis scales have been adjusted for each figure to highlight the quality of pressure reconstruction; thus Figs. 8(a) and (b) have nearly two orders of magnitude difference in scale. The first case, shown in Fig. 8, is at  $\psi_{azm} = 180^\circ$ , where the tower is located directly downstream of the launch vehicle. Temporal lag and attenuation of higher frequency fluctuations are evident when comparing the raw

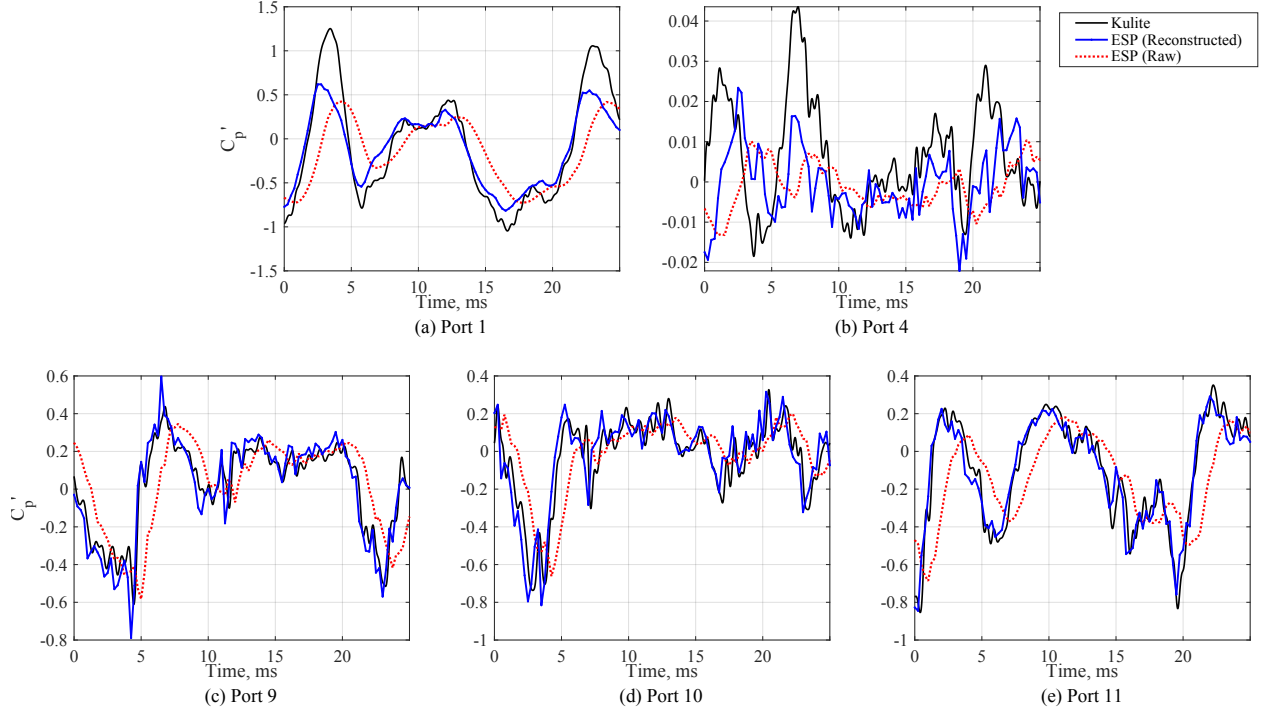


Figure 8. Time domain comparison for high-amplitude pressure fluctuations ( $q_\infty = 50$  psf,  $h/L = -0.003$ , and  $\psi_{azm} = 180^\circ$ ).

ESP and the simultaneously acquired Kulite, such as in Fig. 8(e), where the dashed red line consistently lags the solid black line and has reduced peak amplitude. The pressure results are characterized by relatively high-amplitude fluctuations at all measurement locations except for Port 4, which is located at the stagnation point of the flow. Port 1, located near separation, experiences very strong fluctuations at nearly the same magnitude of the dynamic pressure, and it is not clear whether the lack of good agreement in peak pressure are attributable to the strong gradients in the flowfield, i.e., whether the two sensors compared are experiencing different flow phenomena or the ESP reconstruction is not accurately capturing the physics. Qualitatively, the pressure reconstruction performs very well in recovering the time-series data in Ports 9, 10, and 11. The quality of the comparison is largely dependent on local flow conditions and the associated instrumentation noise that is strongly apparent in the Kulite signals.

Figure 9 demonstrates how each of the signals respond in the lowest-amplitude pressure fluctuation flow environment, at  $\psi_{azm} = 0^\circ$ , where the vehicle is behind the tower with respect to incoming flow. In this case, the vehicle lies within the wake of the launch tower and very weak unsteadiness is observed by the pressure sensors. The first two Kulites, Ports 1 and 4, appear dominated by noise and the ESP comparisons here are very poor. Although instrumentation noise affects all of the Kulites, the effect of noise is substantially lower in Ports 9, 10, and 11, which show good agreement between pairs of sensors even to levels approaching  $p'/q_\infty = 0.01$ . This time-domain comparison provides an initial examination of the signals

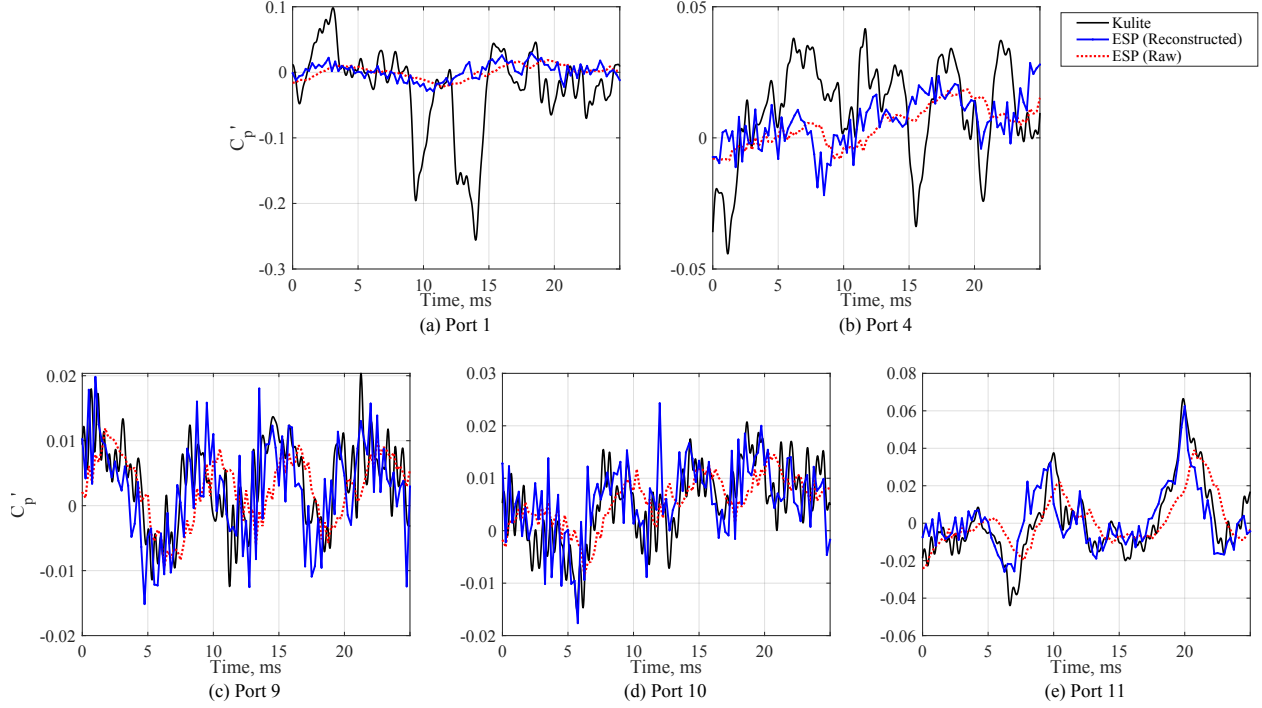


Figure 9. Time domain comparison for low-amplitude pressure fluctuations ( $q_\infty = 50$  psf,  $h/L = -0.003$ , and  $\psi_{azm} = 0^\circ$ ).

measured by the Kulites and those measured by the ESP and reconstructed using the inverse transform methodology, and the reasonable agreement gives confidence that the data are worth additional analysis. The next section will compare the spectral energy distribution between the reconstructed ESP and Kulite pressure signals.

#### 4.1.2 Power Spectral Density (PSD)

The power spectral distribution of pressure at the five comparison locations from a wind tunnel run with high-amplitude pressure fluctuations is plotted in Fig. 10. Despite some concerns regarding noise in the Kulites, these surface-mounted sensors will be considered as the “truth” measurement of the pressure fluctuations on the model surface, and the reconstructed ESP will ideally match the Kulite spectra. As expected, the reconstructed ESP signals shown in Fig. 10 perform well in recovering the frequency content in the three sensor pairs with better time history agreement (Ports 9, 10, and 11), but the PSDs for the first two sensor pairs (Ports 1 and 4) deviate significantly from the Kulite. The noise floor obtained from a wind-off run is included for both Kulite and ESP in these figures - note that the Kulite noise floor is nearly an order of magnitude higher throughout the frequency range for Ports 1 and 4 than for Ports 9, 10, and 11, which are nearly equivalent to the noise in the reconstructed ESP signal at frequencies above 100 Hz. The difference in the noise floor measured in Kulite signals is due to the different Kulite models installed in Ports 1 and 4 and those installed in Ports 9, 10, and 11 (see Section 2.5).

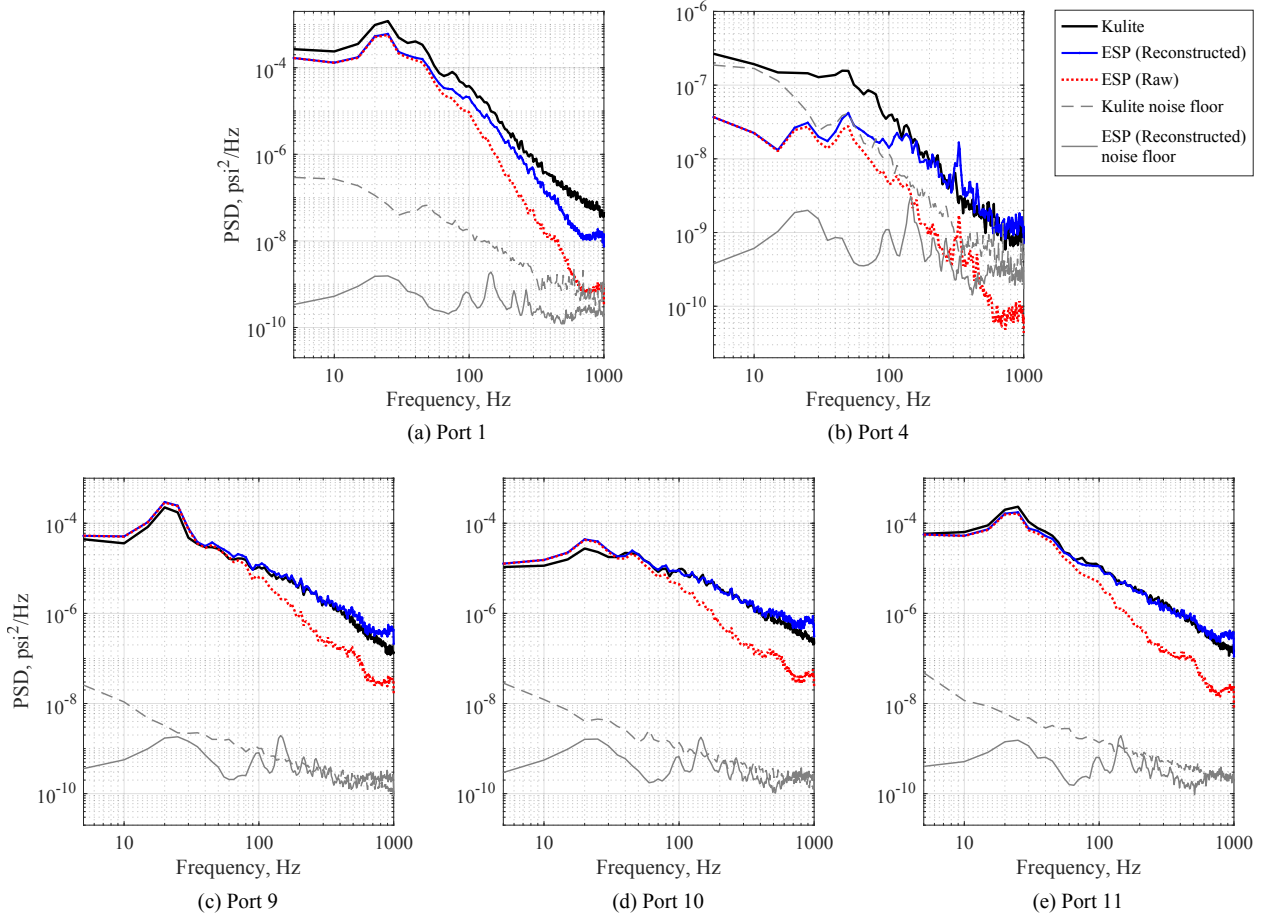


Figure 10. Power spectral density (PSD) comparison for high-amplitude fluctuations ( $q_\infty = 50$  psf,  $h/L = -0.003$ , and  $\psi_{azm} = 180^\circ$ ).

Port 1, which is located approximately  $90^\circ$  from the incoming flow at  $\psi_{azm} = 180^\circ$ , is dominated by low-frequency pressure fluctuations likely associated with separation. As evidenced in the time history for Port 1 plotted in Fig. 8(a), the Kulite measures higher amplitude fluctuations than the reconstructed ESP throughout the frequency range. Since the Kulite and ESP are at a high-gradient region on the surface, it is reasonable to expect a less-than-perfect match in the measured spectra. The Kulite and reconstructed ESP at stagnation, Fig. 10(b), show agreement only above 100 Hz, and the PSD is at similar amplitude as the wind-off noise floor, indicating that the sensor is not resolving the pressure signal from the flow at this flow condition. The three sensors near the tower (Fig. 10(c-e)) all show reasonably good agreement between the ESP and Kulite up to nearly 700 Hz, where the ESP shows higher energy than measured by the Kulite. There is no physical cause that would be expected to produce this shift, and it is reasonable to attribute this behavior to aliasing present in the ESP signal (see Appendix A). The energy distributed across a broad range of frequencies at Ports 9, 10, and 11 is indicative of fully-separated flow behind the vehicle, although the tower influence has a strong impact on the

wake development. Peak amplitude for Ports 1, 9, 10, and 11 is observed between 20 and 25 Hz, which is notable because the blade passage frequency at this wind tunnel operating condition is 26.1 Hz.<sup>1</sup> The strongest fluctuations occur slightly below the associated wind tunnel blade passage frequencies, but this appears to be more of a coincidence than indicative of any clear connection to unsteadiness measured on the model, as discussed in Section 4.2.2.

### 4.1.3 Magnitude-squared Coherence ( $\gamma^2$ )

Quantitative comparison in the frequency domain can be performed by examining the magnitude-squared coherence ( $\gamma^2$ ) and calculating an FRF between each sensor pair. All discussion of ESP signals henceforth will be on the reconstructed signal, since the interest is in the performance of the reconstruction in recovering the pressure fluctuations at the surface of the pressure tap. The coherence between the Kulite and reconstructed ESP signals shows the strength of the linear dependence of the signals from each of the 5 sensor pairs and is plotted for the case with high intensity pressure fluctuations in Fig. 11. The signals for Ports 9, 10, and 11 are very strongly coherent ( $\gamma^2 > 0.9$ ) until approximately 200 Hz, and significant coherence ( $\gamma^2 > 0.5$ ) is observed until approximately 700 Hz. Port 1 shows a dramatic decrease in coherence above 100 Hz, and Port 4 demonstrates relatively weak coherence throughout the frequency range resolvable by the ESP. This can be attributed to the low SNR and the impact of sensor noise in the Kulite at Port 4, which does not affect the other sensors as significantly. For comparison and to further observe SNR impact on the sensors, coherence in the case with weak pressure fluctuations is plotted in Fig. 12. Ports 9, 10, and 11 show significant coherence above approximately 200 Hz and indicates that even in the presence of weak pressure signal, the ESP signal continues to be linearly related to the Kulite.

### 4.1.4 Frequency Response Function (FRF)

While coherence provides the level of linearity between pairs of signals, an FRF quantifies the gain and phase relationship between the two signals and provides a quantitative comparison for how well the reconstructed ESP signal approximates the signal measured by the Kulite at each frequency between 10 Hz and 1,000 Hz. Since the FRF calculation only makes sense for signals that are well-correlated, only the sensor pairs with reasonably high coherence levels are included. For the high-amplitude case, Port 4 is excluded from the FRF calculation due to noise contamination, and for the low-amplitude case, both Ports 1 and 4 are excluded. The gain magnitudes (Figs. 13(a) and 14(a)) are plotted in decibels with the Kulite signal as reference, e.g., a constant line at 0 dB would indicate a perfect match between the amplitude of the ESP signal and the Kulite at all frequencies. Consistent with the PSD plotted in Fig. 10, Port 1 shows a reduction in gain across all frequencies with significant reduction in amplitude above 200 Hz. Ports 9, 10, and 11 show excellent gain agreement (within  $\pm 1$  dB) until above 500 Hz, which also corresponds to

---

<sup>1</sup>The drive motor frequency at  $q_\infty = 50$  psf is approximately 180 rpm, and so with 9 blades, the resulting blade passage frequencies lie between 26 - 28 Hz.

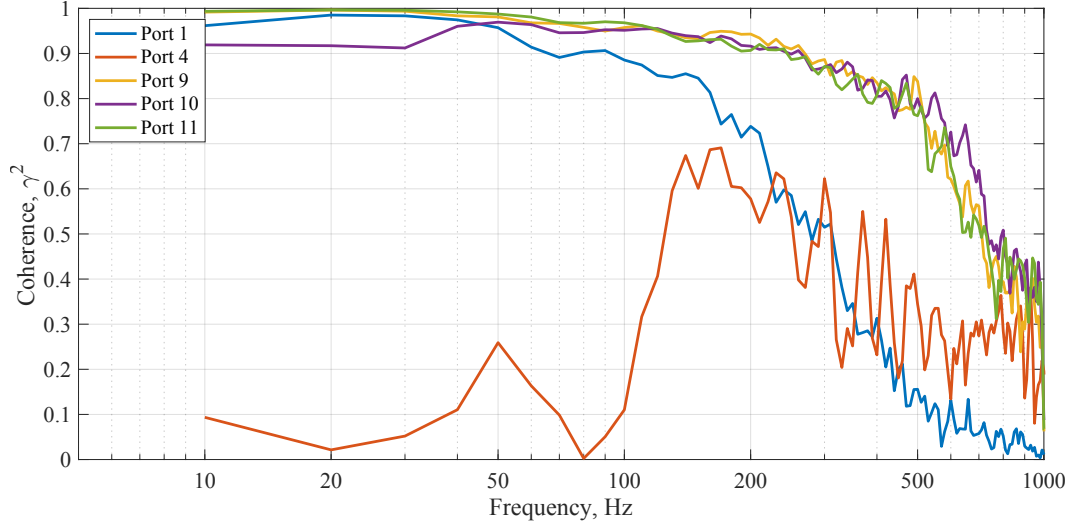


Figure 11. Magnitude-squared coherence of pressure for high-amplitude fluctuations ( $q_\infty = 50$  psf,  $h/L = -0.003$ , and  $\psi_{azm} = 180^\circ$ ).

the decrease in coherence observed in Fig. 11. This indicates that the ESP signals provide accurate representation of the pressure fluctuations measured by the Kulites. The phase behavior (Fig. 13(b)) shows that the ESP significantly lags the Kulite at Port 1 above 200 Hz, which corresponds with the reduction in coherence and potentially shows that the signals are 1) measuring different flow phenomena at this high-gradient location despite the close physical proximity of the sensors or 2) the Kulite noise is strongly contributing to the signal. The maximum phase lag at Ports 9, 10, and 11 is approximately  $60^\circ$  at 1 kHz, which is approximately  $160 \mu\text{s}$  in physical time.

Similar comparisons are observed in the FRF for the case with low-amplitude pressure fluctuations in Figs. 14, but with less agreement observed between each Kulite and reconstructed ESP signals. The reduction in SNR produces worse results in gain, with increased attenuation of the ESP signals with respect to the Kulite, although comparable phase behavior is observed. It is not clear how much of the discrepancy in gain is attributable to noise in the Kulite sensors, which would tend to artificially increase the amplitude of signals measured by the Kulites compared to the ESP, which even after reconstruction demonstrates lower sensor noise. These results offer high confidence that the ESP accurately measures the relevant pressure fluctuations on the surface of the model and the reconstruction process effectively corrects the signal for attenuation and phase lag produced by the tubing system.

## 4.2 Flow Physics

The pressure fluctuations on the surface of the vehicle provide valuable insight into the flow physics observed in the wind tunnel test. The primary quantities of interest will be the distributed pressure intensity, denoted as  $\sigma$  and calculated as the root-mean-square of mean-subtracted pressure fluctuations normalized by  $q_\infty$ , and PSD

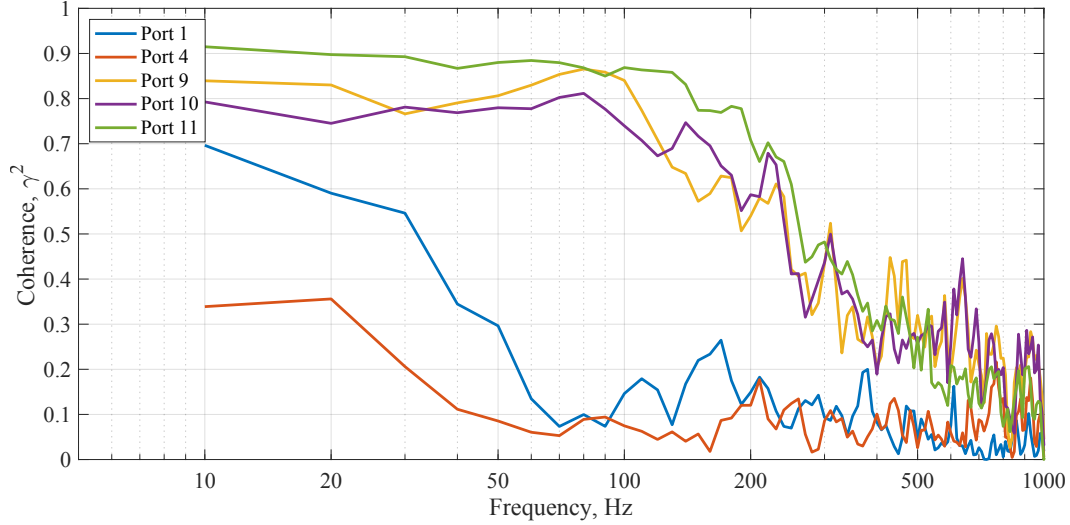
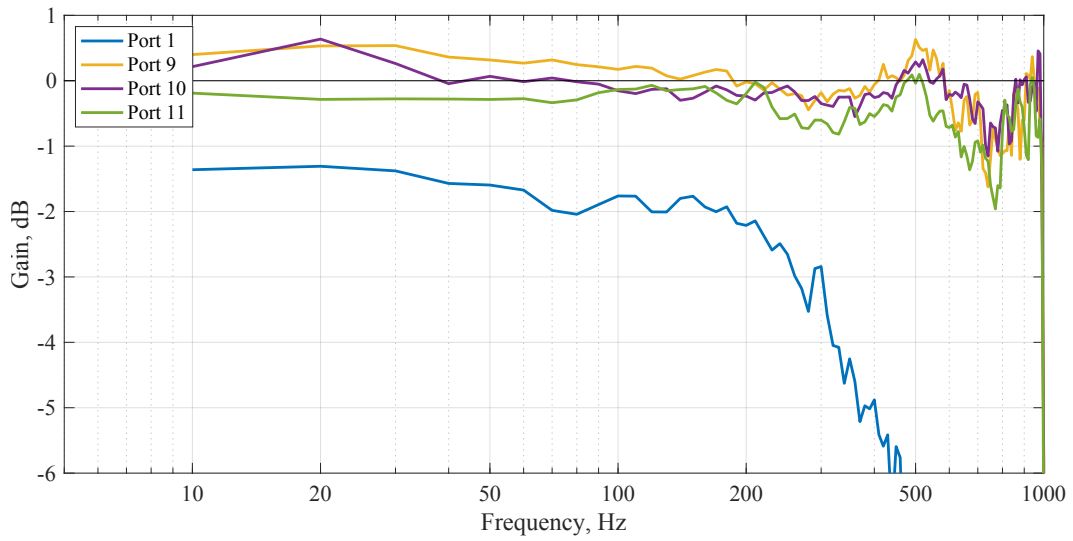


Figure 12. Magnitude-squared coherence of pressure for low-amplitude fluctuations ( $q_\infty = 50$  psf,  $h/L = -0.003$ , and  $\psi_{azm} = 0^\circ$ ).

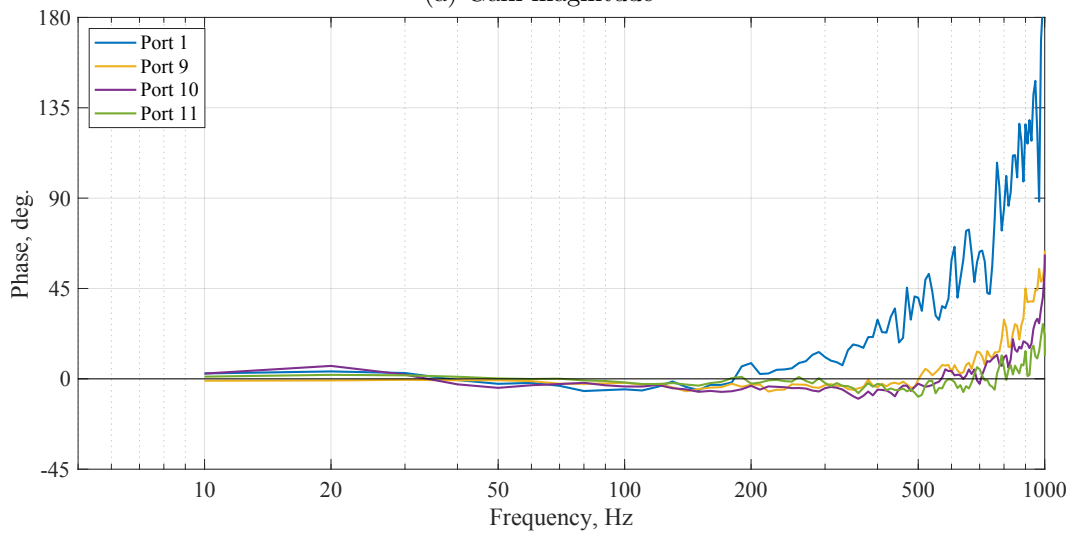
for the three configurations tested. A new variable,  $\theta$ , is introduced to display the surface pressure with respect to the incoming flow direction such that  $\theta = 0^\circ$  always corresponds with the stagnation point of the flow, assuming the vehicle is a circular cylinder (see Fig. 3). This permits a more intuitive comparison when examining the flow physics at different incoming flow angles, since the nominal stagnation point defined by the incoming flow direction is always “clocked” to  $\theta = 0^\circ$ . In addition to variations in  $\psi_{azm}$  and  $h/L$ , the flowfield differences at three vehicle and ML-2 configurations (C1, C2, and C3) will be examined as well.

#### 4.2.1 Pressure Intensity

The overall fluctuation intensity at each measurement location can be displayed as a 2-D contour plot with the incoming flow angle,  $\psi_{azm}$ , plotted on the abscissa and pressure sensor location,  $\theta$ , on the ordinate axis. Each figure contains data from 33 separate data acquisition runs as the model is rotated through a sweep of  $\psi_{azm}$ . As noted previously, flow angles from  $80^\circ$  to  $100^\circ$  were not measured due to mechanical constraints, and these angles are hashed out in the figures. Plotting is limited (“clipped”) to  $\sigma = 0.2$  in order to provide a visually distinctive range and facilitate useful comparisons to cases with weaker unsteadiness. Any clipping in the figure is noted with a black chevron; the maximum level observed in the test was  $\sigma = 0.27$ . Figure 15 shows the distribution of pressure intensity at  $h/L = -0.003$  for C1, where the launch vehicle sits at the ground plane. The strongest pressure fluctuations are noted at  $h/L = -0.003$  and  $\psi_{azm} = 180^\circ$ , where the ML-2 is immediately downstream of the vehicle. These peaks are located at  $\theta = \pm 90^\circ$ , close to where separation would be expected on the sides of the vehicle. A region of very low pressure fluctuations occurs at  $\theta = 0^\circ$ , near the stagnation point of the flow. An additional region of relatively high pressure intensity is observed near  $\theta =$

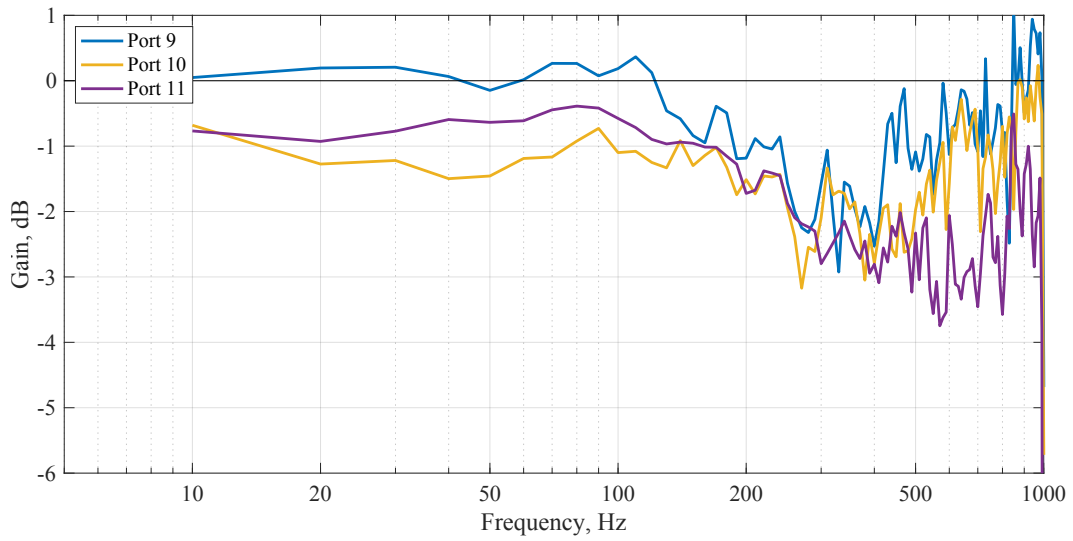


(a) Gain magnitude

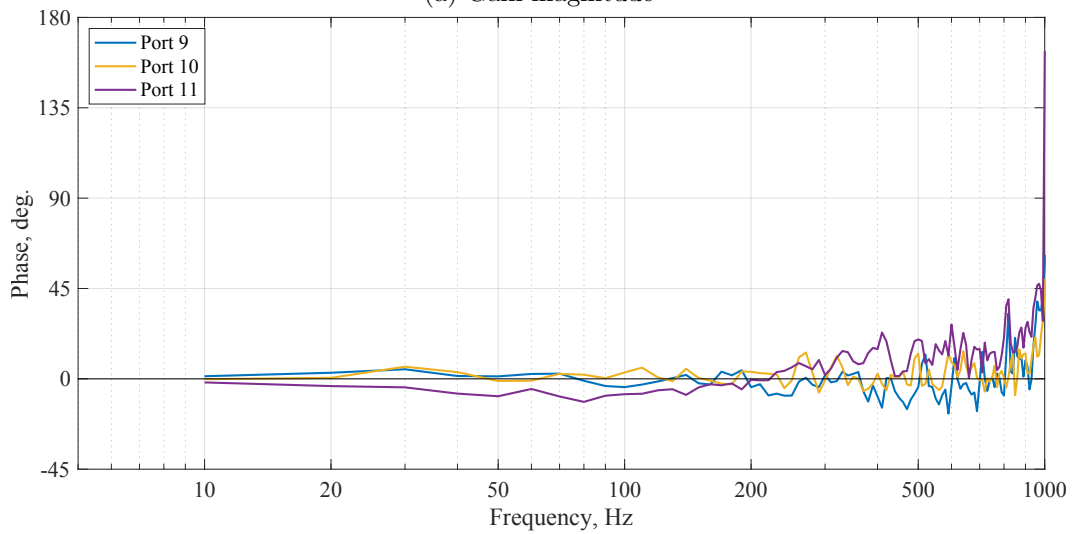


(b) Phase lag

Figure 13. FRF for high-amplitude fluctuations ( $q_\infty = 50$  psf,  $h/L = -0.003$ , and  $\psi_{azm} = 180^\circ$ ).



(a) Gain magnitude



(b) Phase lag

Figure 14. FRF for low-amplitude fluctuations ( $q_\infty = 50$  psf,  $h/L = -0.003$ , and  $\psi_{azm} = 0^\circ$ ).

-120° at  $\psi_{azm} = 330^\circ$ , where shedding from the tower is the likely source of relatively high unsteadiness on the surface of the vehicle. Near  $\psi_{azm} = 0^\circ$ , pressure is very low for all pressure ports because the flow passes through the ML-2 before reaching the vehicle, effectively reducing the fluctuations in the flowfield.

The next figures show the change in  $\sigma$  with increasing vertical elevation of the vehicle relative to the height of the tower,  $h/L$ . As  $h/L$ , is increased from -0.003 to 0.1, the pressure fluctuations reduce significantly, as shown in Fig. 16. Some unsteadiness is observed at  $\psi_{azm} = 180^\circ$  and  $\theta = \pm 90^\circ$ , as well as  $\psi_{azm} = 320\text{-}330^\circ$ , but at less than half the intensity observed at  $h/L = -0.003$ . The results at  $h/L = 0.2$  (Fig. 17) appear very similar to  $h/L = 0.1$ , but with increased pressure fluctuations at  $\psi_{azm} = 330^\circ$ . At  $h/L = 0.3$  (Fig. 18), pressure fluctuations increase, especially at  $\psi_{azm} = 360^\circ$  where the tower is upstream of the vehicle, because at this height, the shear layer produced by the flow over the top of the tower impinges near the axial location of the pressure sensors. Figure 19 shows that the magnitude of pressure fluctuations is observed at  $h/L = 0.4$  is similar to  $h/L = 0.2$  (Fig. 17) and much lower than  $h/L = 0.3$  (Fig. 18). At vehicle heights of  $h/L = 0.5$  (Fig. 20) and above, the influence of the tower becomes negligible at the measurement locations and the results appear similar to those of C3 (no tower), with low unsteadiness except at  $\theta = \pm 90^\circ$ . At the maximum height,  $h/L = 0.876$  (Fig. 21), unsteadiness is observed at  $\psi_{azm} = 300^\circ$ , and although the vehicle is nearly clear of the launch tower (and the pressure port array is far outside direct influence of the tower), this seems to be an effect from the tower and is not observed in the C3 cases. Since the ML-2 is not present in C3, negligible differences in  $\sigma$  are observed with variation in  $h/L$ . The distributions in  $\sigma$  for C3 at  $h/L = -0.003$  and  $h/L = 0.876$  (Fig. 22 and Fig. 23) are nearly identical.

Figure 24 shows the pressure intensity for C2, which has umbilicals deployed between the ML-2 and the SLS vehicle. The overall distribution of  $\sigma$  is very similar to C1 at  $h/L = -0.003$  (Fig. 15). The strongest fluctuations appear at  $\psi_{azm} = 180^\circ$ , but overall intensity is reduced compared to C1, indicating that the wake interaction associated with highest unsteadiness is disrupted by the presence of the deployed umbilicals in the gap between the vehicle and tower.

The next section will examine the PSD for specific cases of interest identified by strong pressure intensity,  $\sigma$ , to observe the frequency distribution.

#### 4.2.2 Power Spectral Density (PSD)

Identifying how pressure fluctuations are distributed by frequency can provide important information on the flow physics present for different model orientations and configurations. Peaks in spectral energy are clearly observed in Fig. 25, which shows the spatial distribution of surface pressure fluctuations at each frequency for the C1 configuration with highest pressure fluctuations at  $\psi_{azm} = 180^\circ$  and  $h/L = -0.003$ . The bright yellow regions at 22.5 Hz wrap around the circumference of the model (from -180° to +180°) and are especially strong at  $\pm 90^\circ$ , corresponding to the prominent peaks in line plots of PSD in Fig. 10. Minimal fluctuations across all frequencies occur at the flow stagnation point, near  $\theta = 0^\circ$ , and attached flow on the surface of the model produces low energy within high-frequency regions (above 100

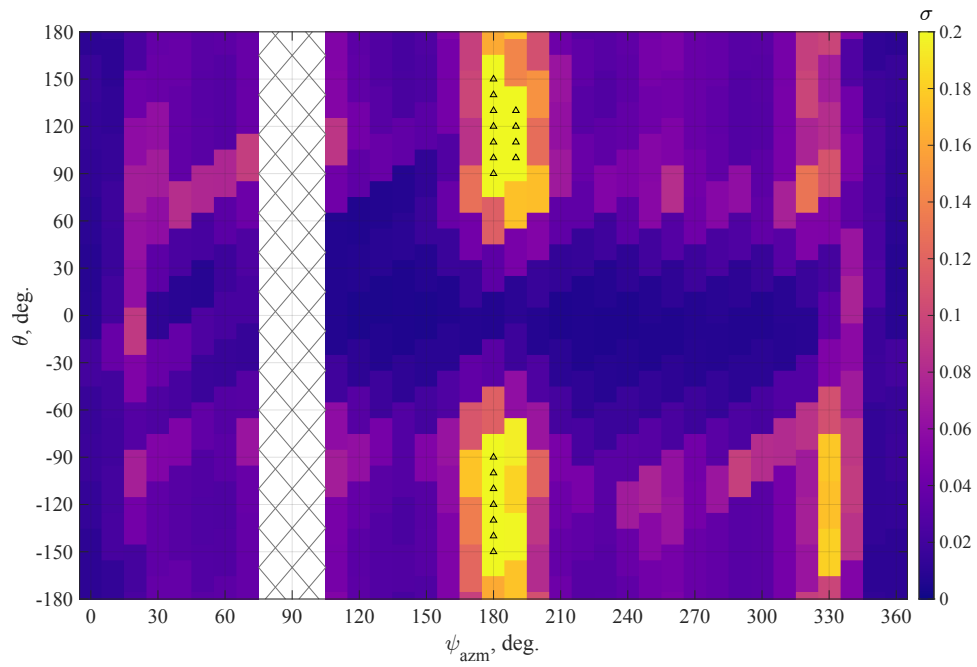


Figure 15. Pressure intensity ( $\sigma$ ) for C1 at  $h/L = -0.003$ . Black chevrons indicate levels of  $\sigma > 0.2$ .

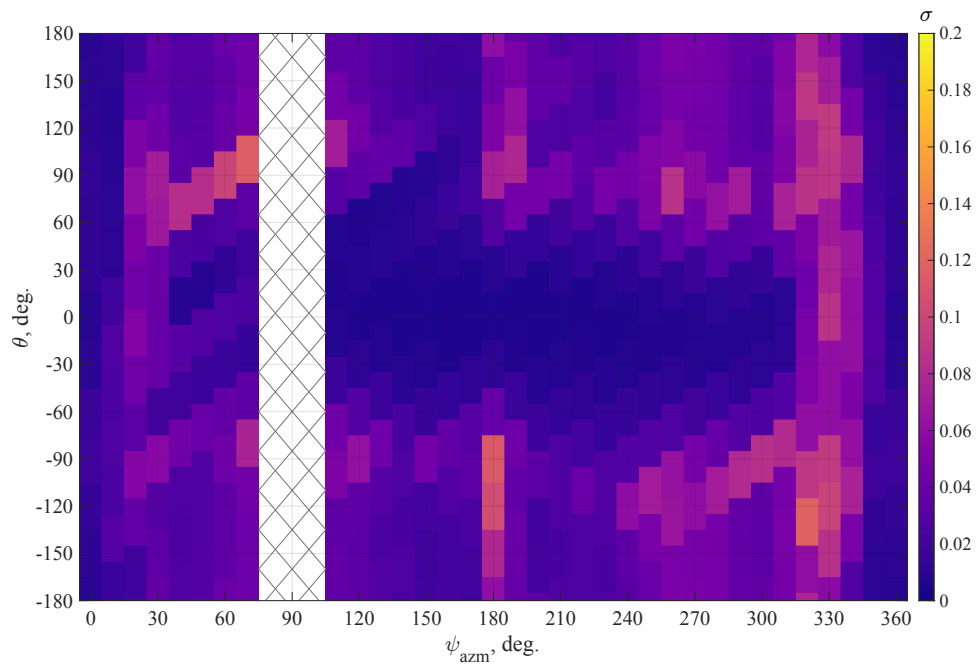


Figure 16. Pressure intensity ( $\sigma$ ) for C1 at  $h/L = 0.1$ .

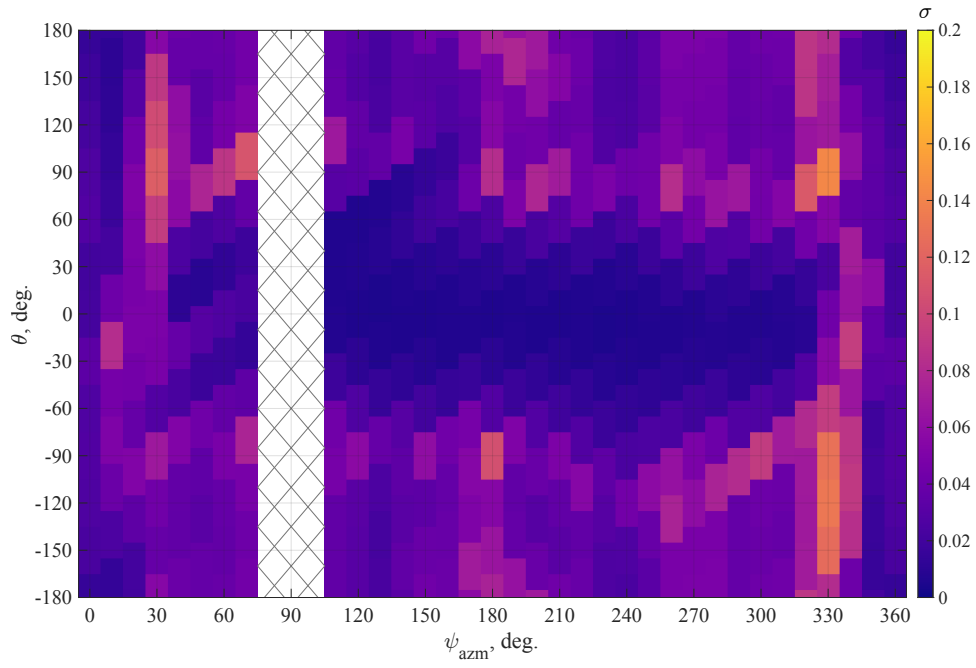


Figure 17. Pressure intensity ( $\sigma$ ) for C1 at  $h/L = 0.2$ .

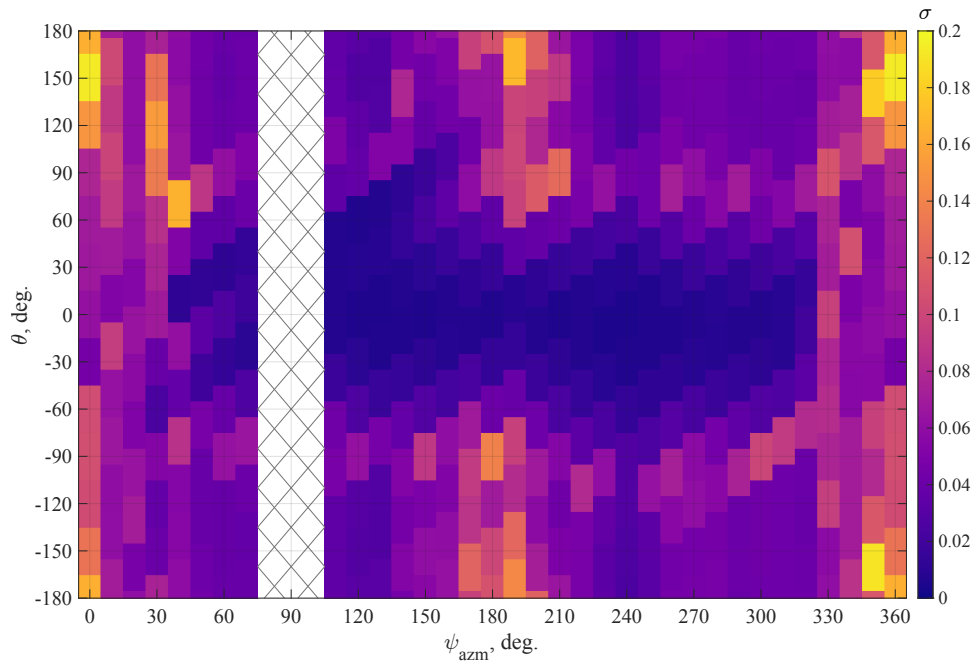


Figure 18. Pressure intensity ( $\sigma$ ) for C1 (with tower) at  $h/L = 0.3$ .

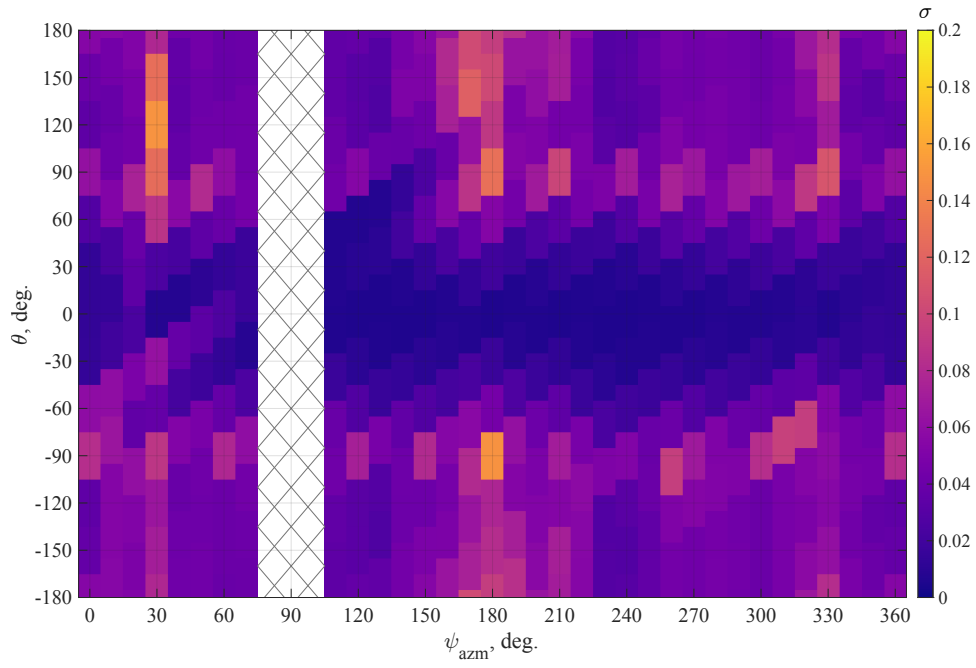


Figure 19. Pressure intensity ( $\sigma$ ) for C1 (with tower) at  $h/L = 0.4$ .

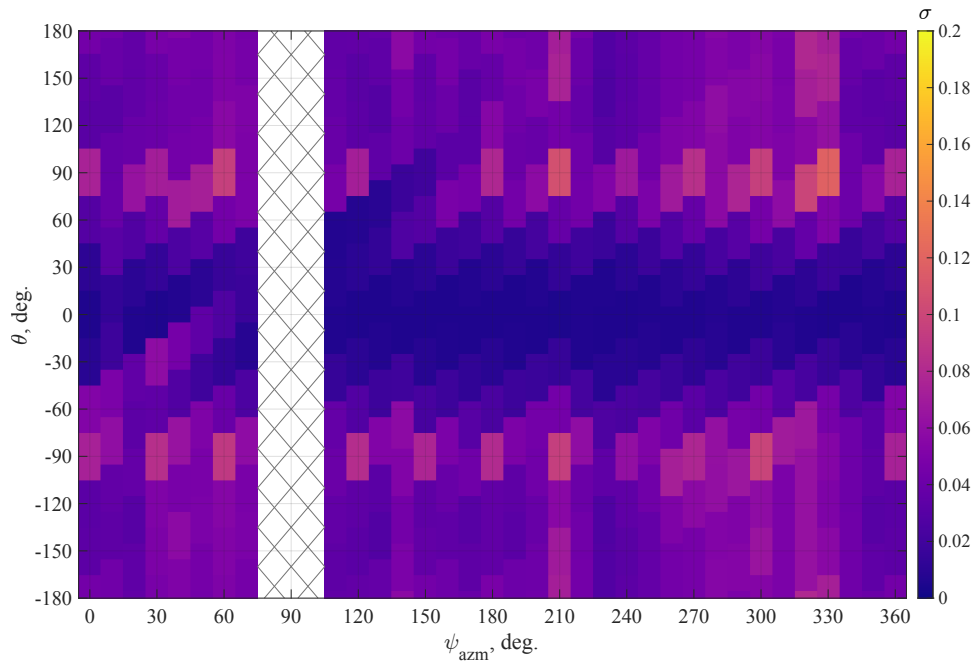


Figure 20. Pressure intensity ( $\sigma$ ) for C1 (with tower) at  $h/L = 0.5$ .

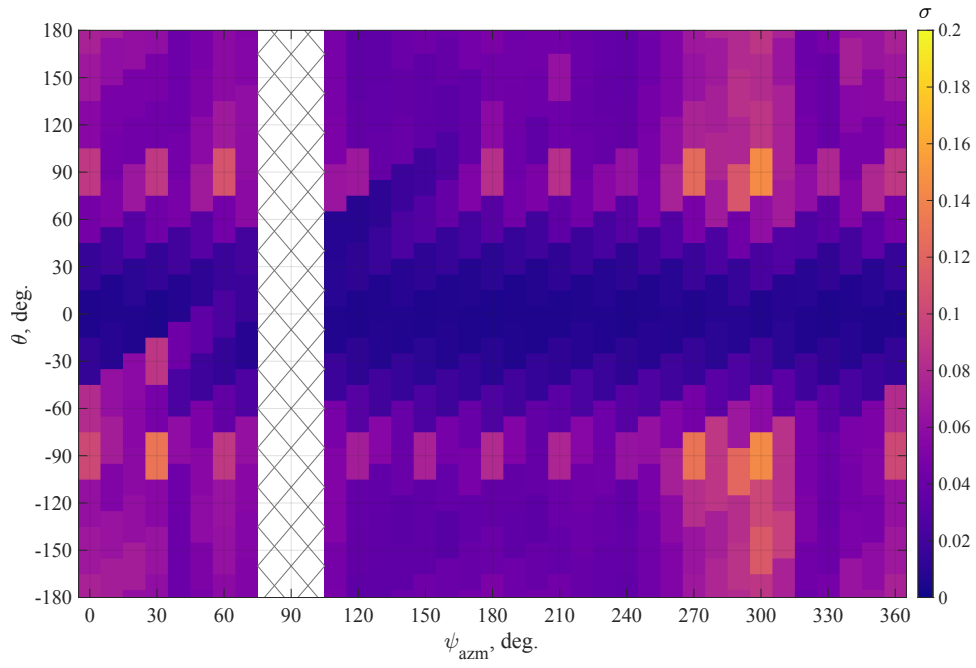


Figure 21. Pressure intensity ( $\sigma$ ) for C1 at  $h/L = 0.876$ .

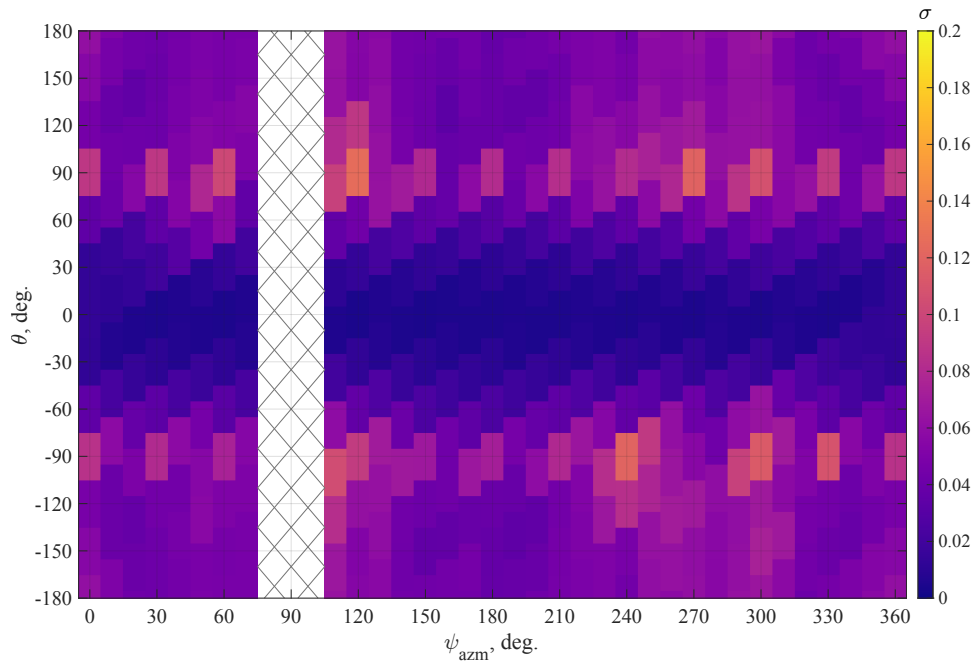


Figure 22. Pressure intensity ( $\sigma$ ) for C3 (no tower) at  $h/L = -0.003$ .

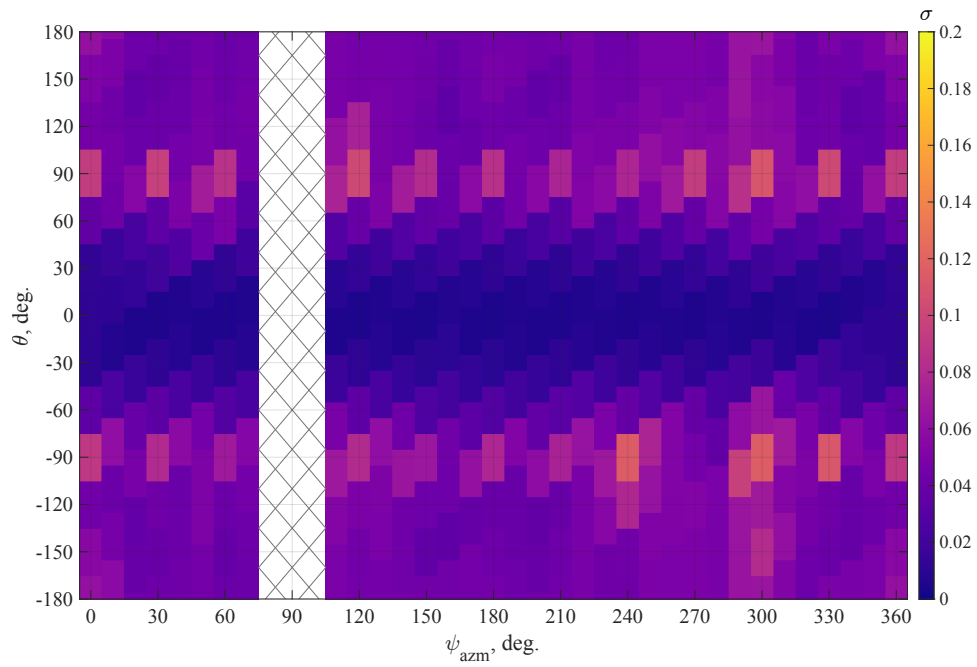


Figure 23. Pressure intensity ( $\sigma$ ) for C3 at  $h/L = 0.876$ .

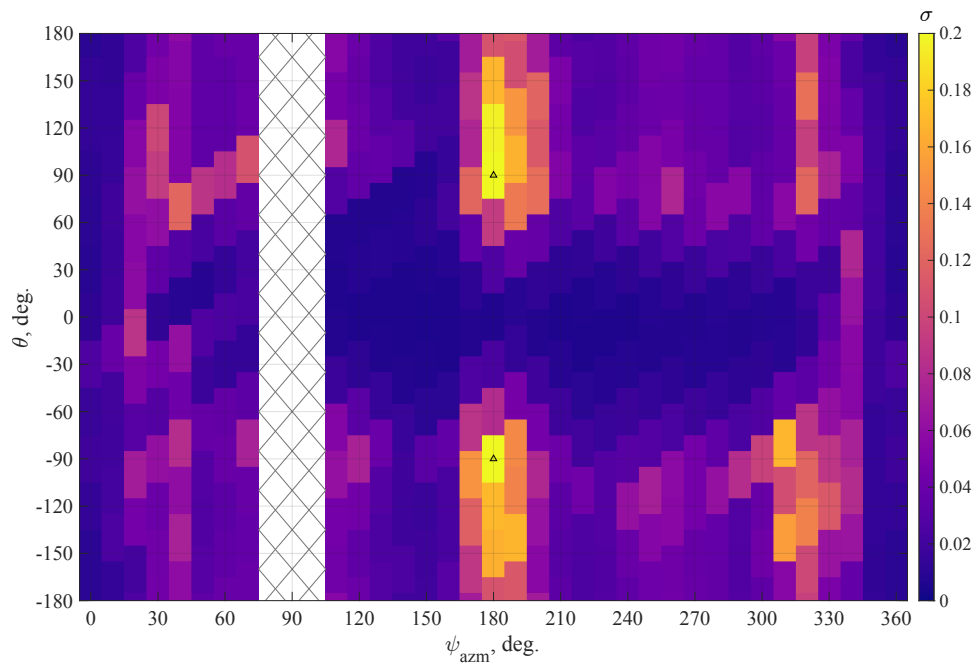


Figure 24. Pressure intensity ( $\sigma$ ) for C2 (with tower and umbilicals) at  $h/L = -0.003$ . Black chevrons indicate levels of  $\sigma > 0.2$ .

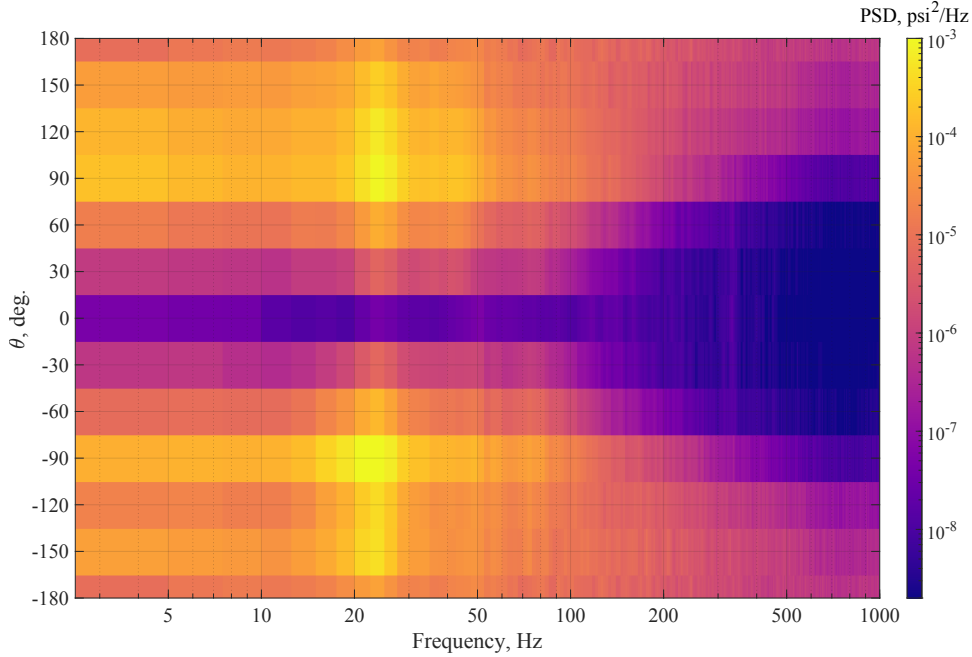


Figure 25. Distribution of PSD for C1 at  $\psi_{azm} = 180^\circ$  and  $h/L = -0.003$ .

Hz) between  $\theta = \pm 90^\circ$  centered at  $0^\circ$ . The broadband distribution between  $\theta = \pm 120^\circ$  centered at  $180^\circ$  indicates fully separated flow between the vehicle and tower.

The same flow conditions are tested for C2, shown in Fig. 26, which includes the deployed umbilicals between the ML-2 and launch vehicle. The peak frequency increases to 27.5 Hz and overall intensity is lower than observed in C1, and apparent harmonics are also visible around 55 Hz and 82.5 Hz. Both configurations can be compared to experiments with only the launch vehicle (Fig. 27), with similar distribution in frequency to C1 and C2. Strong fluctuations at  $\theta = \pm 90^\circ$  indicate the onset of separation and fully separated flow behind the vehicle produces a broad distribution of frequencies. The most significant difference between the cases with and without the tower present is that no peak frequencies appear without the tower, suggesting that the strong fluctuations are a coupled effect created by a wake interaction between the vehicle and tower. It is not clear how the wake interaction, which occurs in the gap between the vehicle and tower, produces pressure fluctuations that are apparent in the attached flow at the front of the vehicle, between  $\theta = \pm 60^\circ$ .

The complex flowfield that exists in the wake interaction between two generic bluff bodies is difficult to predict from a fundamental physics perspective, let alone for complex geometries such as a cylindrical launch vehicle with protuberances and a semiporous truss structure. The PSD without the tower (Fig. 27) shows no coherent vortex shedding at any particular frequency, indicative of flow within the transcritical regime, using the terminology of Szechenyi [14]. The dramatic increase and tonal nature of the fluctuating pressure observed with blockage in the wake of the vehicle (Figs. 25 and 26) is a potential indication of resonant flow features occurring in the gap between two bodies, albeit at lower frequencies and at smaller

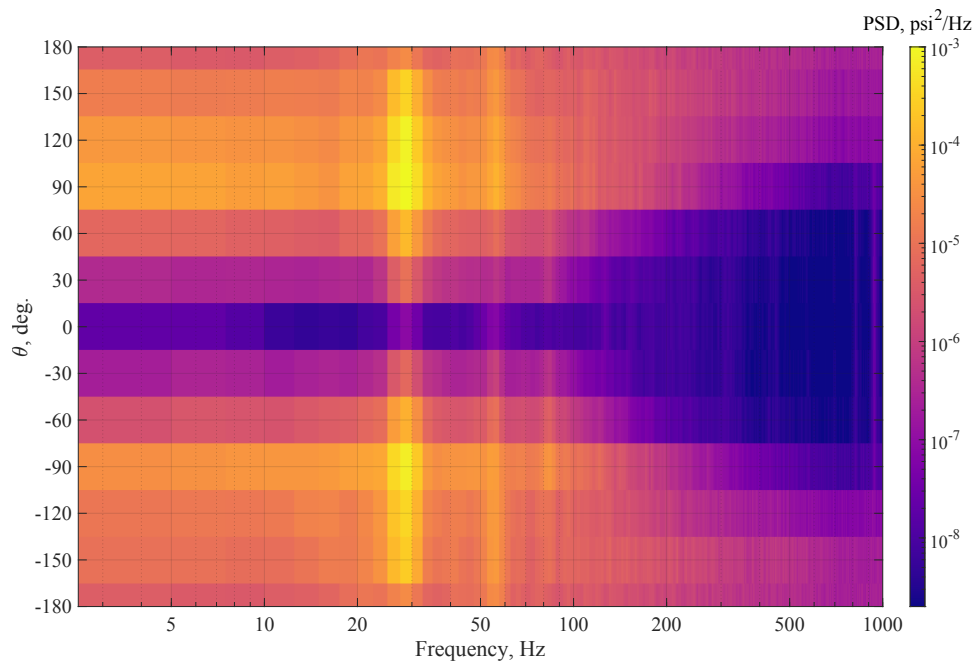


Figure 26. Distribution of PSD for C2 at  $\psi_{azm} = 180^\circ$  and  $h/L = -0.003$ .

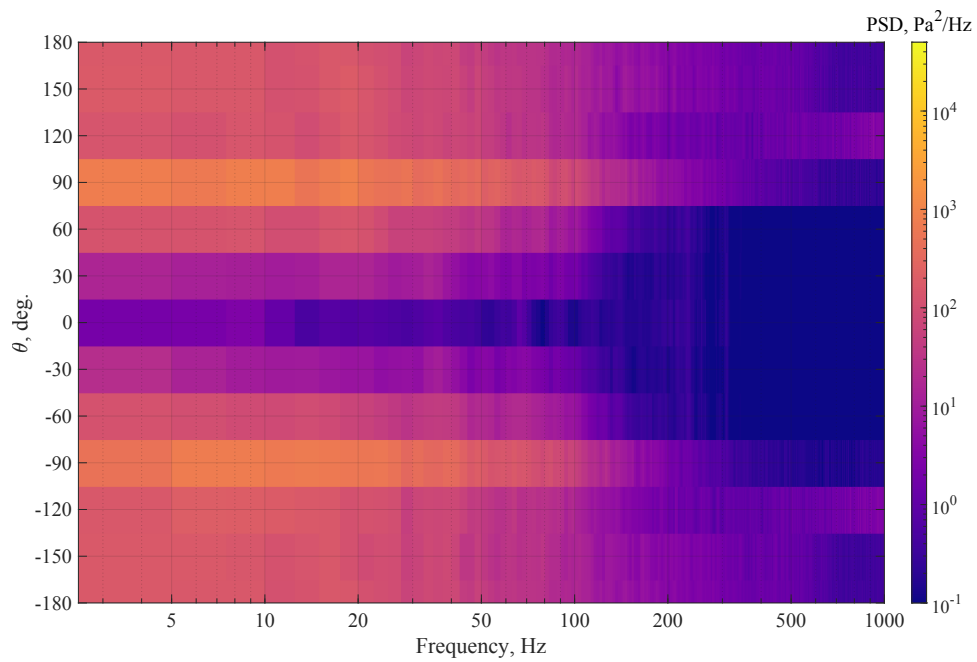


Figure 27. Distribution of PSD for C3 at  $\psi_{azm} = 180^\circ$  and  $h/L = -0.003$ .

gap spacings than observed in tandem cylinder studies in the subcritical flow regime,  $Re_D$  less than  $0.2 \times 10^6$  [15]. The Strouhal number of the 22.5 Hz peak in Fig. 25 using the cylinder diameter  $D$  ( $St_D$ ) equals 0.051, while the Strouhal number using the gap between the vehicle and the tower is 1.28 times higher (0.066) - neither of which appear physically meaningful in single or tandem cylinder flow studies. Treating the gap as a cavity and estimating Rossiter tones for the gap geometry yields expected frequencies in excess of 100 Hz [16], much higher than the fundamental frequencies observed. It is possible that cavity-like shear layer excitation and acoustic resonance from the wake interaction with the tower are responsible for the strong pressure fluctuations that are felt upstream of flow separation on the vehicle surface, but the current measurements do not provide conclusive evidence of the underlying flow phenomena. Although surface pressure measurements are not sufficient for definitive characterization of the flow physics, the current study can help guide future flowfield measurements to determine the mechanism driving the amplification in unsteady pressure.

## 5 Conclusions and Recommendations

The current study achieved both goals of validating a novel method for measuring unsteady pressure using instrumentation typically limited to time-averaged measurements and observed interesting flow physics present in the wind tunnel test. The pressure reconstruction methodology developed by Resono and implemented in the present test produced an accurate reconstruction of pressure fluctuations on the surface of the model, where 5 of the 12 total pressure taps included Kulites for validation purposes. Despite noise contamination and low SNR in the Kulite signals, good agreement was observed up to frequencies of approximately 500 Hz, where the frequency response of the reconstructed ESP signals remained within 1 dB of the magnitude ratio and within  $10^\circ$  of the phase of the Kulite signals for cases with the strongest pressure fluctuations (highest SNR).

Future considerations for validating the technique include application to compressible flows, different test species (such as R-134a refrigerant), and large temperature differences. Supersonic and hypersonic tests involve large differences in test gas properties when running, and it is not presently known how much variations in gas properties between the tubing characterization step and running a test will affect the quality of the reconstruction process and measurement accuracy. Additional efforts by Resono include uncertainty quantification of the reconstructed pressure based on the SNR of the measured signals and uncertainty in the tubing geometry parameters required to develop the inverse transform function.

The strong oscillations observed at  $\psi_{azm} = 180^\circ$  for cases with the launch tower present point to complex flow physics that are absent in the vehicle-alone flowfield. The interaction of the vehicle wake with the tower shows potential cavity-flow-like characteristics, such as coherent fluctuations, and these measurements can help guide future studies to better understand the dynamical behavior of the flow structures present in the gap between the cylindrical vehicle and the truss-like tower. Additionally, umbilical systems connecting the tower and launch vehicle appear to

disrupt strong fluctuations and increase the fundamental frequency slightly. These observations will be useful in interpreting force and moment measurements made in the present wind tunnel test and determining the applicability of the observed flow patterns to the liftoff environment of the full-scale SLS vehicle.

## References

1. Whitmore, S. A., Lindsey, W. T., Curry, R. E., and Gilyard, G. B., “Experimental Characterization of the Effects of Pneumatic Tubing on Unsteady Pressure Measurements,” NASA TM 4171, National Aeronautics and Space Administration, 1990.
2. Whitmore, S. A. and Leondes, C. T., “Pneumatic Distortion Compensation for Aircraft Surface Pressure Sensing Devices,” *Journal of Aircraft*, Vol. 28, No. 12, 1991, pp. 828–836.
3. Whitmore, S. A. and Fox, B., “Improved Accuracy, Second-Order Response Model for Pressure Sensing Systems,” *Journal of Aircraft*, Vol. 46, No. 2, 2009, pp. 491–500.
4. Nikoueeyan, P., Hind, M., Strike, J., Singh, M., Naughton, J. W., Keeter, S., and Dahland, M., “Characterization of Unsteady Pressures on a Blunt Trailing Edge Using a Direct-Mount Pressure Scanner,” *AIAA Scitech 2019 Forum*, 2019, pp. 1–13.
5. Strike, J., Hind, M., Saini, M., Naughton, J. W., Wilson, M., and Whitmore, S. A., “Unsteady Surface Pressure Reconstruction on an Oscillating Airfoil Using the Wiener Deconvolution Method,” *27th AIAA Aerodynamic Measurement Technology and Ground Testing Conference*, 2010, p. 4799.
6. Mier, F. A., Nikoueeyan, P., Perry, M., Hind, M., and Naughton, J. W., “Characterizing Remotely Acquired Pressure Measurements from Shock Tube Experiments,” *AIAA SciTech 2022 Forum*, 2022, p. 2172.
7. Chan, D. T., Paulson, J. W., Shea, P. R., Toro, K. G., Parker, P. A., and Commo, S. A., “Aerodynamic Characterization and Improved Testing Methods for the Space Launch System Liftoff and Transition Environment,” *AIAA AVIATION Forum 2019*, 2019, pp. 1–35.
8. Neuhart, D. H. and McGinley, C. B., “Free-Stream Turbulence Intensity in the Langley 14- by 22-Foot Subsonic Tunnel,” NASA TP 213247, National Aeronautics and Space Administration, 2004.
9. Gentry Jr, G. L., Quinto, P. F., Gatlin, G. M., and Applin, Z. T., “The Langley 14-by 22-foot Subsonic Tunnel: description, flow characteristics, and guide for users,” NASA TP 3008, National Aeronautics and Space Administration, 1990.
10. Anonymous, “National Instruments 9239,” [https://www.ni.com/pdf/manuals/375939b\\_02.pdf](https://www.ni.com/pdf/manuals/375939b_02.pdf), 2016, Accessed August 23, 2021.

11. Bergh, H. and Tijdeman, H., “Theoretical and Experimental Results for the Dynamic Response of Pressure Measuring Systems,” NLR-TR F.238, Amsterdam Nationaal Luchtvaarlaboratorium (National Aeronautical and Astronautical Research Institute), 1965.
12. Whitmore, S. A. and Wilson, M. D., “Wiener Deconvolution for Reconstruction of Pneumatically Attenuated Pressure Signals,” *AIAA Journal*, Vol. 49, No. 5, 2011, pp. 890–897.
13. Anonymous, “Matlab Resample Documentation,” <https://www.mathworks.com/help/signal/ref/resample.html>, 2020, Accessed November 19, 2021.
14. Szechenyi, E., “Supercritical Reynolds Number Simulation for Two-Dimensional Flow Over Circular Cylinders,” *Journal of Fluid Mechanics*, Vol. 70, 1975, pp. 529–542.
15. Neuhart, D. H., Jenkins, L., Choudhari, M., and Khorrami, M., “Measurements of the Flowfield Interaction between Tandem Cylinders,” *15th AIAA/CEAS Aeroacoustics Conference (30th AIAA Aeroacoustics Conference)*, 2009, p. 3275.
16. Rossiter, J. E., “Wind-Tunnel Experiments on the Flow over Rectangular Cavities at Subsonic and Transonic Speeds,” R. and M. No. 3438, Aeronautical Research Council, 1964.

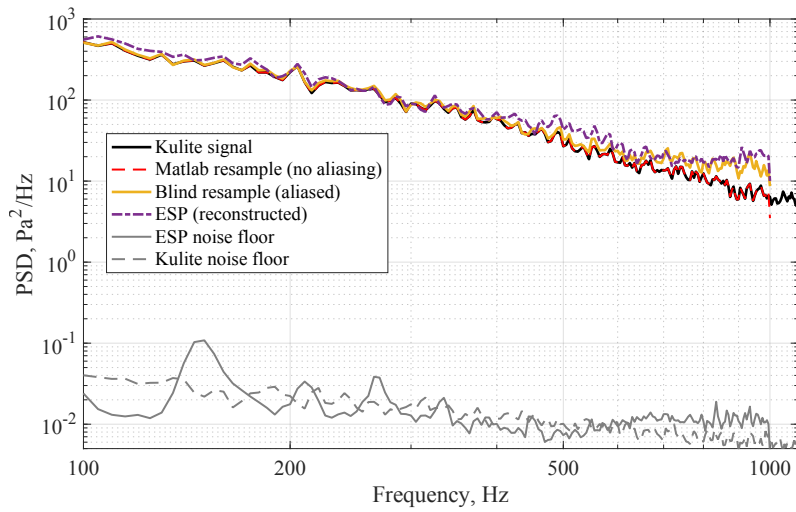
# Appendix A

## Potential Effects of Aliasing

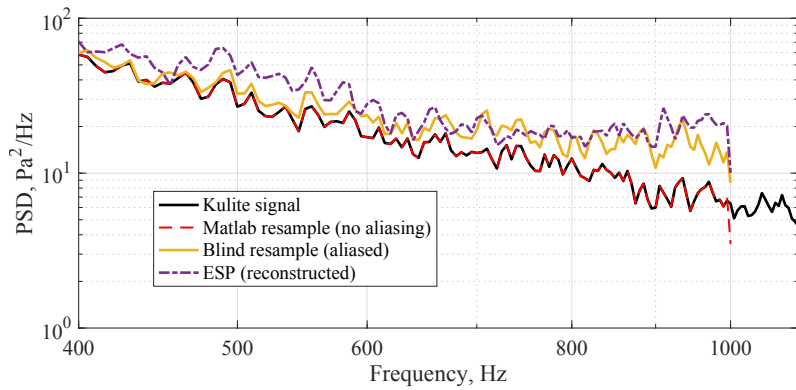
In order to investigate whether aliasing is a potential cause for the increase in energy in the reconstructed ESP signals (Section 4.1.2), the signals from the Kulites are artificially downsampled in order to introduce aliasing and make direct comparisons to the reconstructed ESP signals. Downsampling is necessary because the Kulites are acquired at  $f_s = 50$  kHz, while the ESP records pressure at  $f_s = 2$  kHz – a multiple of 25. The signals are decimated using two methods: 1) Matlab’s built-in `resample` function [13], which automatically applies Finite Impulse Response (FIR) lowpass filtering when performing operations to reduce sample size, and 2) blind resampling, which simply selects every 25th element from the time series to reduce the effective sampling rate, but introduces aliasing since no filtering is applied. The results are plotted for two flow conditions in Fig. A1 to highlight the effect of SNR on the comparison between Kulite and ESP signals.

The case with high SNR is plotted in Fig. A1(a), and the noise floor calculated from wind-off data is included to show that even at 1,000 Hz, the PSD is approximately 3 orders of magnitude greater than the noise floor. The original Kulite signal is plotted with the black solid line, and the Matlab `resample` signal is plotted with the red dashed line. As described in Section 3.2, a high-order filter (order 10,000) is selected to preserve spectral content up to nearly 1,000 Hz. The spectral content of the black and red lines is identical until 990 Hz, where roll-off due to filtering becomes evident, but as expected, no aliasing is introduced. Blindly resampling the Kulite data (yellow line) introduces higher spectral energy to the signal, with significant increase observable at 1,000 Hz. Figure A1(b) shows a zoomed region of the PSD for better clarity. Here, the reconstructed ESP (purple line) closely follows the PSD of the blindly resampled Kulite, which is affected by aliasing, rather than the original or filtered resampled Kulite, which are not affected by aliasing.

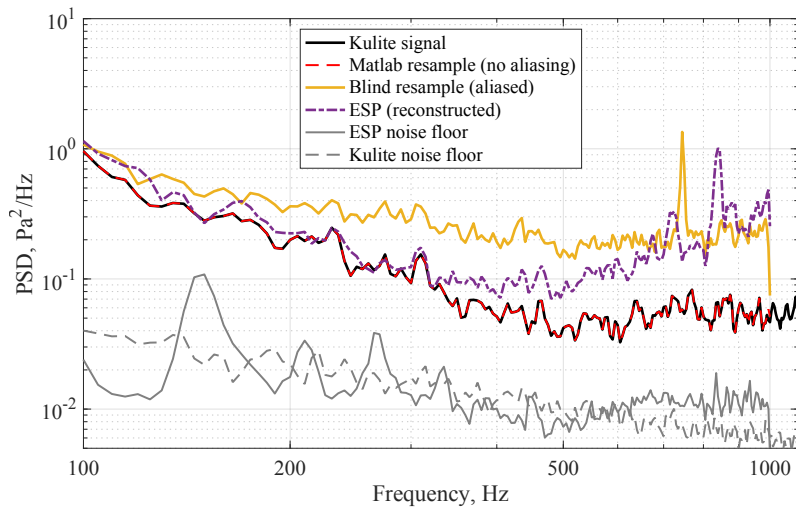
A case with very low SNR is included in Fig. A1(c). Significant departure from the original signal is observed at a different frequency based on the SNR - in Fig. A1(b), this occurs near 500 Hz, whereas in Fig. A1(c), deviations between the blindly resampled data and the original signal can be observed below 200 Hz. Similarly, the reconstructed ESP signal follows the increase of spectral energy of the blindly resampled Kulite data above 600 Hz in Fig. A1(b), while the ESP signal deviates from original Kulite data above 300 Hz in Fig. A1(c). Additionally, a peak is introduced at nearly 800 Hz in the blindly resampled Kulite data that is not present in the original signal – this is likely a result of instrumentation noise that has been aliased onto the frequency band. These findings should be taken into consideration when interpreting the PSD and reliable bandwidth attributed to the ESP data, which is dependent on local flow conditions and SNR. Given high enough SNR, the impact of aliasing seems negligible - unless significant phenomena occur at frequencies above 1,000 Hz, which would have an impact on lower frequencies. Because of this, it is assumed that peaks at relatively high frequencies occurring in low SNR cases, like in Fig. A1(c), are not realistic.



(a)  $\psi_{azm} = 180^\circ$  (High SNR)



(b)  $\psi_{azm} = 180^\circ$  (High SNR), zoomed to 400 - 1,000 Hz



(c)  $\psi_{azm} = 0^\circ$  (Low SNR)

Figure A1. Original and resampled signals demonstrating potential effects of aliasing.

## Appendix B

### Noise Analysis

The quality of data comparison is largely dependent on local flow features present on the vehicle, since cases with very little pressure fluctuation are more influenced by noise, which can be quantified as signal-to-noise ratio (SNR). Many no-flow, wind-off cases were recorded throughout the test campaign, which provides a rich quantitative view of the inherent noise present in the system.

Significant energy during wind-off measurements was observed in the Kulite signals, which produced two characteristic noise profiles corresponding to the two models used in the experiment. The Kulites had different in-line amplifiers during fabrication and were only observed in the present experiment thanks to the high bit depth (24-bit) of the NI-DAQ modules.

A series of wind-off measurements colored by individual Kulite sensors is included in Fig. B1. The measurements show good repeatability over the test series, and two distinct noise characteristics are observed in the spectra. This can be attributed to the two distinct in-line amplifiers used in the Kulite models XCL-19 and XCL-31, which have different cut-off frequencies. There is significant correlated noise at higher frequencies, but this is not significant below 1 kHz, which is the maximum resolvable frequency of the ESP module and as such is the maximum frequency considered in the present analysis. The lower noise present in the XCL-31 sensors makes these the preferred choice when calculating FRF and establishing accuracy of the signals measured with the ESP.

The ESP noise can be evaluated similarly. In Fig. B2, both the raw signal measured by the ESP transducer (solid lines) and the reconstructed (dotted lines) signal are plotted for each channel for a single wind-off data point. The 12 raw channels follow nearly identical noise floor characteristics, and the only significant deviation in reconstructed signals occurs at the line that is pinched (ESP Port 12). The data from this port are not included in subsequent analysis because of the severe attenuation observed. One important note is that the signal reconstruction that eliminates signal attenuation at higher frequencies also increases the noise floor, but the overall level of the noise remains low across the frequency range measured. SNR will be an important consideration when making quantitative comparisons in the performance of the two acquisition methods.

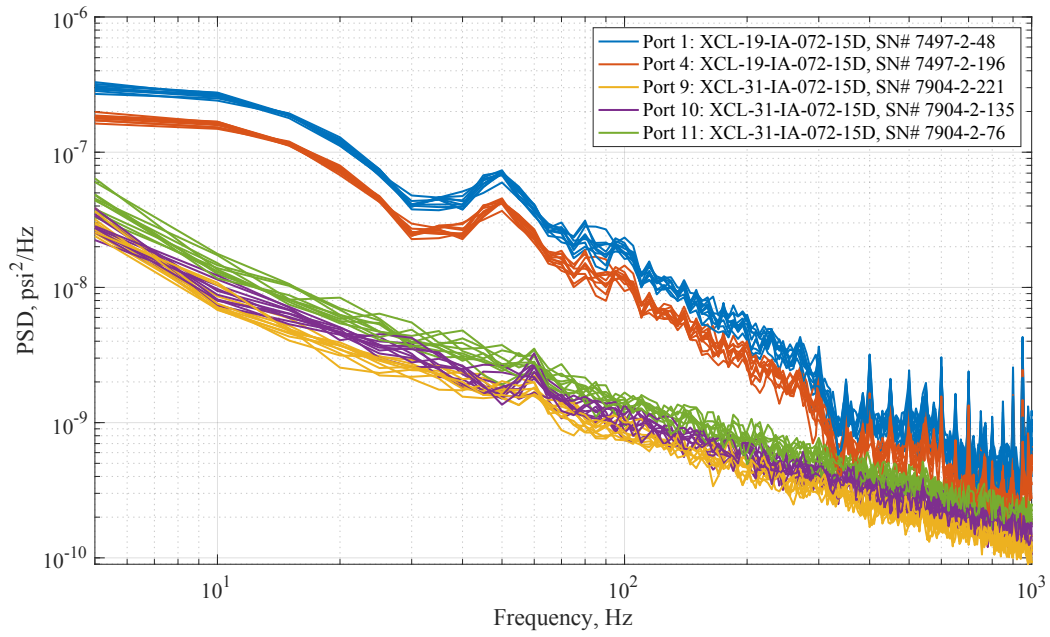


Figure B1. Kulite measurements at wind-off conditions.

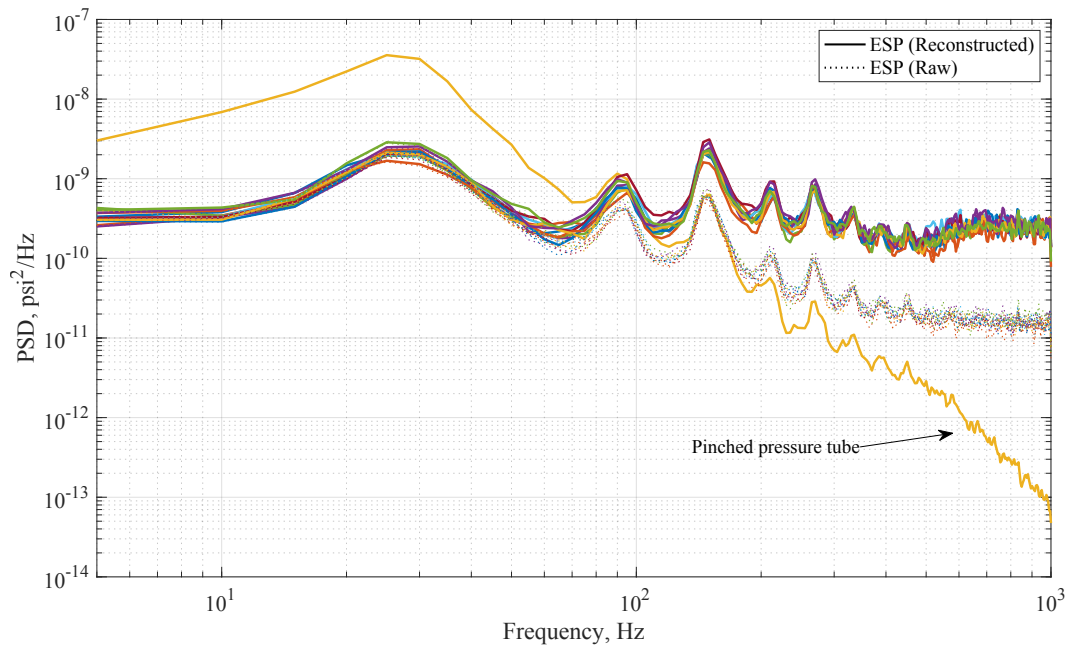


Figure B2. ESP measurements at wind-off conditions.

**REPORT DOCUMENTATION PAGE**

*Form Approved  
OMB No. 0704-0188*

The public reporting burden for this collection of information is estimated to average 1 hour per response, including the time for reviewing instructions, searching existing data sources, gathering and maintaining the data needed, and completing and reviewing the collection of information. Send comments regarding this burden estimate or any other aspect of this collection of information, including suggestions for reducing this burden, to Department of Defense, Washington Headquarters Services, Directorate for Information Operations and Reports (0704-0188), 1215 Jefferson Davis Highway, Suite 1204, Arlington, VA 22202-4302. Respondents should be aware that notwithstanding any other provision of law, no person shall be subject to any penalty for failing to comply with a collection of information if it does not display a currently valid OMB control number.  
**PLEASE DO NOT RETURN YOUR FORM TO THE ABOVE ADDRESS.**

<b>1. REPORT DATE (DD-MM-YYYY)</b> 01-03-2022		<b>2. REPORT TYPE</b> Technical Memorandum		<b>3. DATES COVERED (From - To)</b>	
<b>4. TITLE AND SUBTITLE</b> Unsteady Pressure Acquisition on the 1.75% Scale SLS Block 1B Cargo Liftoff Configuration				<b>5a. CONTRACT NUMBER</b> SAA-34369	
				<b>5b. GRANT NUMBER</b>	
				<b>5c. PROGRAM ELEMENT NUMBER</b>	
<b>6. AUTHOR(S)</b> Mears, L. J.; Shea, P. R., Collins, J. G., Walker, M. A., Langston, S. L., Pinier, J. T.; Nikoueeayan, P.; Naughton, J.; Perry, M.; Strike, J.; Wimpenny, B., Hind, M.				<b>5d. PROJECT NUMBER</b>	
				<b>5e. TASK NUMBER</b>	
				<b>5f. WORK UNIT NUMBER</b>	
<b>7. PERFORMING ORGANIZATION NAME(S) AND ADDRESS(ES)</b> NASA Langley Research Center Hampton, Virginia 23681-2199				<b>8. PERFORMING ORGANIZATION REPORT NUMBER</b> L-X	
<b>9. SPONSORING/MONITORING AGENCY NAME(S) AND ADDRESS(ES)</b> National Aeronautics and Space Administration Washington, DC 20546-0001				<b>10. SPONSOR/MONITOR'S ACRONYM(S)</b> NASA	
				<b>11. SPONSOR/MONITOR'S REPORT NUMBER(S)</b> NASA/TM-20220002633	
<b>12. DISTRIBUTION/AVAILABILITY STATEMENT</b> Unclassified-Unlimited Subject Category 34 Availability: NASA STI Program (757) 864-9658					
<b>13. SUPPLEMENTARY NOTES</b> An electronic version can be found at <a href="http://ntrs.nasa.gov">http://ntrs.nasa.gov</a> .					
<b>14. ABSTRACT</b> Time-varying pressure on the core of the Space Launch System (SLS) Block 1B Cargo vehicle was acquired using instrumentation typically used for steady, time-averaged pressure. Resono Pressure Systems, Inc. in partnership with the University of Wyoming have developed a unique hardware and software system for measuring unsteady pressure, which was implemented in a large-scale wind tunnel test through a nonreimbursable Space Act Agreement with NASA. The technique was applied to 12 pressure ports on the 1.75% scale SLS wind tunnel model. Tubing lengths of approximately 14 inches separated the pressure transducer module from the pressure taps on the model surface, and surface-mount validation sensors (Kulites) were installed in close proximity to 5 of the 12 pressure ports. Up to about 500 Hz, the frequency response of pressure fluctuations agreed to within 1 dB of amplitude and 10° of phase difference compared to the simultaneously-acquired surface-mount transducers. Sample results using the reconstructed pressure from the full azimuthal ring of taps are presented.					
<b>15. SUBJECT TERMS</b> unsteady pressure, flow measurement					
<b>16. SECURITY CLASSIFICATION OF:</b>			<b>17. LIMITATION OF ABSTRACT</b>  UU	<b>18. NUMBER OF PAGES</b>  37	<b>19a. NAME OF RESPONSIBLE PERSON</b> STI Information Desk ( <a href="mailto:help@sti.nasa.gov">help@sti.nasa.gov</a> )
<b>a. REPORT</b>  U	<b>b. ABSTRACT</b>  U	<b>c. THIS PAGE</b>  U			<b>19b. TELEPHONE NUMBER (Include area code)</b> (757) 864-9658